Bioactive Materials 36 (2024) 490–507

Contents lists available at ScienceDirect

Bioactive Materials

journal homepage: www.keaipublishing.com/en/journals/bioactive-materials

ROS-responsive and triple-synergistic mitochondria-targeted polymer micelles for efficient induction of ICD in tumor therapeutics

Xiaoxiao Hu [a,1], Mo Zhang [a,**,1], Cuilu Quan [a], Saisai Ren [a], Wei Chen [b,c,d,*], Jing Wang [a,***]

[a] School of Pharmacy, Key Laboratory of Innovative Drug Development and Evaluation, Hebei Medical University, No.361 Zhongshan East Road, Shijiazhuang, 050017, PR China
[b] Department of Orthopaedic Surgery, The Third Hospital of Hebei Medical University, No.139 Ziqiang Road, Shijiazhuang, 050051, PR China
[c] Key Laboratory of Biomechanics of Hebei Province, Orthopaedic Research Institution of Hebei Province, No.139 Ziqiang Road, Shijiazhuang, 050051, PR China
[d] NHC Key Laboratory of Intelligent Orthopaedic Equipment, The Third Hospital of Hebei Medical University, No.139 Ziqiang Road, Shijiazhuang, 050051, PR China

ARTICLE INFO

Keywords:
Immunogenic cell death
Mitochondria-targeted
Reactive oxygen species
Photodynamic therapy
Polymer micelle

ABSTRACT

Immunogenic cell death (ICD) represents a modality of apoptosis distinguished by the emanation of an array of damage-related molecular signals. This mechanism introduces a novel concept in the field of contemporary tumor immunotherapy. The inception of reactive oxygen species (ROS) within tumor cells stands as the essential prerequisite and foundation for ICD induction. The formulation of highly efficacious photodynamic therapy (PDT) nanomedicines for the successful induction of ICD is an area of significant scientific inquiry. In this work, we devised a ROS-responsive and triple-synergistic mitochondria-targeted polymer micelle (CAT/CPT-TPP/PEG-Ce6, CTC) that operates with multistage amplification of ROS to achieve the potent induction of ICD. Utilizing an "all-in-one" strategy, we direct both the PDT and chemotherapeutic units to the mitochondria. Concurrently, a multistage cyclical amplification that caused by triple synergy strategy stimulates continuous, stable, and adequate ROS generation (domino effect) within the mitochondria of cells. Conclusively, influenced by ROS, tumor cell-induced ICD is effectively activated, remodeling immunogenicity, and enhancing the therapeutic impact of PDT when synergized with chemotherapy. Empirical evidence from in vitro study substantiates that CTC micelles can efficiently provoke ICD, catalyzing CRT translocation, the liberation of HMGB1 and ATP. Furthermore, animal trials corroborate that polymer micelles, following tail vein injection, can induce ICD, accumulate effectively within tumor tissues, and markedly inhibit tumor growth subsequent to laser irradiation. Finally, transcriptome analysis was carried out to evaluate the changes in tumor genome induced by CTC micelles. This work demonstrates a novel strategy to improve combination immunotherapy using nanotechnology.

1. Introduction

Immunogenic cell death (ICD) is a distinctive form of apoptosis marked by the dissemination of various damage-related molecular signals, which inaugurates a novel paradigm for present tumor immunotherapy [1,2]. ICD can reverse the immunogenicity of multifarious cancers and amplify the therapeutic efficacy. At the core of ICD lies the endoplasmic reticulum stress response, which culminates in the translocation of calreticulin (CRT) to the plasma membrane's surface. This phenomenon facilitates the phagocytosis and presentation of tumor antigens by antigen-presenting cells, particularly dendritic cells, thus effectively instigating a specific anti-tumor immune response. The promotive agents for CRT translocation include ROS-regulated endoplasmic reticulum stress arm and PEK-mediated eIF2α protein phosphorylation [3–5]. It becomes evident that the generation of intracellular reactive oxygen species (ROS) constitutes both the prerequisite and the

Peer review under responsibility of KeAi Communications Co., Ltd.
* Corresponding author. Department of Orthopaedic Surgery, The Third Hospital of Hebei Medical University, No.139 Ziqiang Road, Shijiazhuang, 050051, PR China.
** Corresponding author.
*** Corresponding author.
E-mail addresses: 2537893226@qq.com (X. Hu), 19101691@hebmu.edu.cn (M. Zhang), 1925205003@qq.com (C. Quan), 771456951@qq.com (S. Ren), surgeonchenwei@126.com (W. Chen), 17200949@hebmu.edu.cn (J. Wang).
[1] These two authors contributed equally to this work.

https://doi.org/10.1016/j.bioactmat.2024.06.038
Received 24 April 2024; Received in revised form 28 June 2024; Accepted 28 June 2024

foundation for ICD induction [6–10]. Accordingly, researchers have postulated that the oxidative stress of specific organelles within tumor cells may play a decisive role in triggering ICD. Ding et al. pioneered an exploration of the connection between mitochondrial oxidative stress and ICD in 2019, thereby initially elucidating the mechanism of mitochondrial ROS-based oxidative stress behavior in inducing tumor cell ICD and uncovering a close nexus between mitochondria and tumor cell ICD [11]. In summation, the development of drug delivery system predicated on the targeted induction of mitochondrial oxidative stress bears significant implications for the precision treatment of tumors via ICD.

A drug delivery system that substantially augments the production of ROS in tumor cells represents the key challenge to be surmounted to effectually activate ICD. In addition to chemotherapeutic agents such as camptothecin (CPT) that stimulate cells to generate ROS, other treatments like chemodynamic therapy (CDT) [12,13], photothermal therapy (PTT) [14,15], and photodynamic therapy (PDT) [16,17] also induce tumor cells to induce ROS. Of these, PDT has garnered extensive interest due to inherent advantages such as non-invasiveness, reduced drug resistance, and minimal side effects attributable to precise light irradiation [18–22]. Elevated levels of ROS produced by PDT can induce both apoptosis and necrosis in cancer cells and cultivate a specific ROS-rich microenvironment [23–25]. Nonetheless, tumor hypoxia constitutes a barrier to PDT's efficacy, as PDT can swiftly exhaust oxygen (O_2) concentration, exacerbating tumor hypoxia [26–29]. Given the constrained diffusion area and ephemeral lifespan of ROS in PDT, and the pronounced dependence of the therapeutic outcome on O_2 concentration, the sole use of a photosensitizer is inadequate to trigger sufficient CRT translocation to attain optimal immunotherapy.

Integrating photosensitizers with hypoxia mitigation strategies emerges as an efficacious approach for PDT drug systems to enhance ROS generation. He et al. [30] ingeniously conceived and fabricated a novel metal-organic framework drug delivery system (BSA-MnO_2/-Ce6@ZIF-8) characterized by controllable tumor microenvironment interaction. In this construct, ZIF-8 elevates the encapsulation efficiency of Ce6, thus precluding photosensitizer self-aggregation and optimizing PDT efficiency. Additionally, the extensive specific surface area of ZIF-8 permits MnO_2 modification on its surface, allowing for self-generated O_2 under acidic condition, thereby achieving augmented PDT. Similarly, Chen et al. [31] designed a nanosystem (CaO_2@ZIF-Fe/Ce6@PEG) that autonomously supplies H_2O_2/O_2 for enhanced CDT/PDT based on CaO_2 nanoparticles. Within this system, CaO_2 generates Ca^{2+}, H_2O_2, and O_2 in the acidic tumor microenvironment, where Ca^{2+} amplifies oxidative stress and Fe interacts with generated H_2O_2 to mediate CDT; PDT is contingent on photosensitizer presence, requiring O_2 mediation to generate singlet oxygen ($^1O_2$), and the O_2 generation serves to fortify PDT, culminating in efficient cancer treatment. These investigations collectively illustrate that photosensitizers and hypoxia mitigation synergistically engender sufficient ROS under laser irradiation condition. Nevertheless, the limited time for cells or organisms to receive laser irradiation raises the fundamental question of stimulating sustained, stable, and adequate ROS generation in cells, a challenge yet to be resolved for the initiation of effective ICD.

Recognizing the paramount role of mitochondrial oxidative stress in the initiation of ICD, we aimed to achieve continuous, stable, and adequate ROS production within cells to induce and facilitate ICD. To this end, we constructed ROS-responsive and triple-synergistic mitochondria-targeted polymer micelles, to effectively induce ICD, remodel tumor immunogenicity, and enhance the therapeutic effect. This objective was attained by targeting the mitochondria with an integrated strategy of PDT and chemotherapy action units, underpinned by judiciously designed PDT units and the selection of appropriate chemotherapy agents. The ROS-responsive and triple-synergistic mitochondria-targeted polymer micelles in question were obtained via self-assembly of two amphiphilic polymer chains (Chain I and Chain II) (Scheme 1). Chain I is composed of CPT-CA-PEG-TPP, obtained through the esterification of CPT-CA that stimulate mitochondrial ROS production and PEG-modified mitochondrial-targeted molecule triphenylphosphine (TPP) via amidation reaction. Within Chain I, CPT and Cinnamaldehyde (CA) are connected by ROS-responsive bonds (TK and

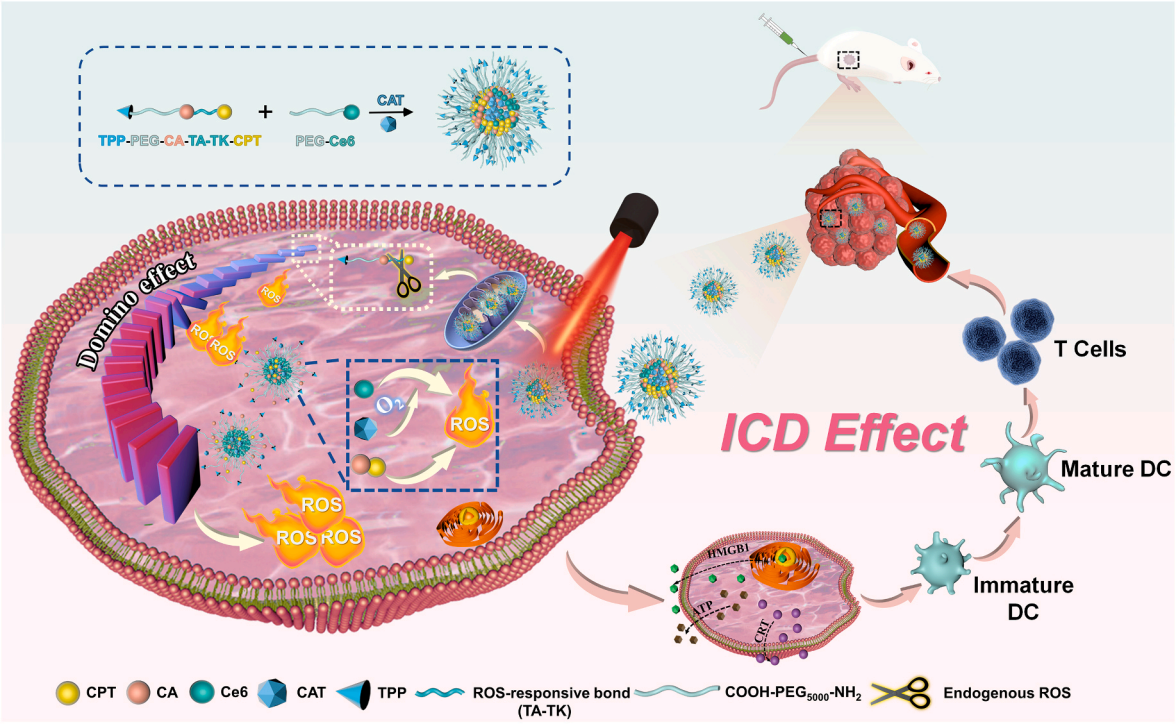

Scheme 1. Schematic diagram of the preparation process of ROS-responsive and triple-synergistic mitochondria-targeted polymer micelles and the effective induction of ICD through domino effect that ROS induced upon entry into cells.

TA bonds). Concurrently, PEG and the photosensitizer chlorin e6 (Ce6) undergo amidation reaction to form PEG-Ce6 (Chain II). These strands I and II self-assemble into polymer micelles via hydrophilic interaction and encapsulate catalase (CAT) within the hydrophobic region during assembly. Upon cellular entry, the micelle targets the mitochondria under TPP's guidance. Within the mitochondrial environment, endogenous ROS partially break the ROS-responsive bonds, leading to the release of certain quantities of CPT, Ce6, and CA. The first module involved in the chain I in the micelles. CPT, in addition to its role as a chemotherapy agent, stimulates ROS production [32–35]; as well as that CA instigates the mitochondria to release ROS [36–38]. The second module (PDT module) was included in chain II in the micelles. Ce6 generates ROS under 660 nm irradiation. The third module included CAT which can induce the formation of O_2 to relieve hypoxia, and then to synergy the PDT.

In summary, ROS-inducing prodrug agents, linked by ROS-responsive bonds, engage the mitochondria, instigating consistent, stable, and ample ROS production within cellular mitochondria through a triple-synergistic strategy to induce a domino effect for multimodal tumor therapy. This leads to the ultimate release of substantial and sustained ROS within the mitochondria, culminating in the translocation of CRT to the surface of plasma membrane, thereby translocation fosters the phagocytosis and presentation of tumor antigens by dendritic cells (DCs), further efficiently initiating specific anti-tumor immune responses and amplifying the overall tumor treatment effects.

2. Experimental section

2.1. Materials

COOH-PEG_{5000}-NH_2 was sourced from Shanghai Ponsure Biotech, Inc. (Shanghai, China). N-hydroxysuccinimide (NHS) and 1-ethyl-(3-dimethylaminopropyl) carbodiimide hydrochloride (EDCI), as well as (5-Carboxypentyl) triphenylphosphonium bromide and 1-hydroxybenzotriazole, were acquired from Macklin Biochemical Co. Ltd (Shanghai, China). Chlorin e6 (Ce6) was obtained from Zhengzhou Alpha Chemical Co., Ltd (Zhengzhou, China). Aladdin Chemical Co., Ltd provided Camptothecin (CPT), Cinnamaldehyde (CA), Catalase (CAT) and 1-Hydroxybenzotriazole (HOBT). Both Dimethyl sulfoxide (DMSO) and triethylamine were obtained from Tianjin Fuyu Chemical Co. Ltd (Tianjin, China). N, N-Dimethylformamide (DMF) was purchased from Tianjin Yongda Chemical Reagent Co. Ltd (Tianjin, China). Diphenylisobenzofuran (DPBF) was procured from J&K Scientific (Beijing, China). Hydrogen peroxide (H_2O_2) was bought from Beijing Chemicals (Beijing, China). 4',6-diamidino-2-phenylindole (DAPI) was purchased from Sigma-Aldrich Trading Co. Ltd (China). Other chemicals, such as 3-(4,5-dimethylthiazol-2-yl)-2,5-diphenyl tetrazolium bromide (MTT), RPMI 1640 culture medium, fetal bovine serum (FBS), penicillin-streptomycin (PS), 2,7-Dichlorodihydrofluorescein diacetate (DCFH-DA), Annexin V-FITC/PI Apoptosis Kit, Calcein-AM, and propidium iodide (PI) were sourced from their respective suppliers as previously detailed. Calreticulin Rabbit Monoclonal Antibody, HMGB1 Rabbit Monoclonal Antibody, Alexa Fluor 488-labeled Goat Anti-Rabbit IgG (H + L), Mitro-Tracker Green, JC-1, Mitro-Tracker red, Lyso-Tracker Green, and ATP and BCA Protein Assay Kit were obtained from Shanghai Beyotime Biotechnology Co. Ltd (Shanghai, China). The anti-CD3-PerCP, anti-CD4-FITC, anti-CD8-PE, anti-CD25-PerCP, anti-FOXP3-PE were purchased from BioLegend (San Diego, CA, USA).

2.2. Preparation of CPT-CA-PEG-TPP (Chain I)

The synthesis process of CPT-CA is delineated in the supporting information. CPT-CA-PEG-TPP was synthesized employing the esterification reaction mechanism. Initially, 5.72 mg of TPP-PEG_{5000}-COOH, 13.24 mg of EDCI, and 12.67 mg of HOBT were dissolved in 1 mL of DMF. Subsequently, 50 μL of triethylamine was introduced to activate the mixture at room temperature for 15 min. After the activation period, 1 mL of CPT-CA (5.60 mg/mL) was incorporated and allowed to react at room temperature for 24 h. The mixture was then dialyzed using a dialysis bag possessing a molecular weight cut-off of 2000, for a period of 72 h. Following dialysis, the supernatant was collected, freeze-dried, and set aside for subsequent utilization.

2.3. Preparation of PEG-Ce6 (Chain II)

The synthesis was performed based on the principle of amidation reaction. Specifically, 6.44 mg of NH_2-PEG_{5000}-COOH, 54.65 mg of NHS, 46.64 mg of EDCI, and 5.21 mg of Ce6 were dissolved in 4 mL of DMSO and stirred at room temperature for 12 h. After this period, dialysis was executed using a dialysis bag with a molecular weight cut-off of 2000, for 72 h, followed by collected and freeze-dried.

2.4. Preparation of polymer micelles

An even mixture was obtained by ultrasonically blending 1 mL of CPT-CA-PEG-TPP (0.82 mg/mL) ethanol solution and 0.8 mL of PEG-Ce6 (0.675 mg/mL) ethanol solution. This mixture was then slowly added dropwise to 3 mL of CAT (0.73 mg/mL) aqueous solution. After droplet addition, the mixture was stirred at room temperature for 9 h. Subsequently, the ethanol was removed using a rotary evaporator (30 °C), followed by centrifugation with water and removal of unloaded CAT to obtain CAT/CPT-TPP/PEG-Ce6 micelles, denoted as CTC micelles. The TPP-free micelles (CNC) and CAT-free micelles (TC) were prepared by the same method. The encapsulation rate of CAT was calculated by the BCA method (encapsulation rate% = amount of CAT loaded/CAT amount of input × 100 %).

2.5. Characterization of polymer micelles

The UV–vis absorption spectra of PEG-TPP and PEG-Ce6 were analyzed using a UV-2700 UV spectrophotometer (Shimadzu Corporation, Japan). FTIR spectra of COOH-PEG_{5000}-NH_2, TPP, Ce6, CPT-CA, PEG-Ce6, PEG-TPP, and CPT-CA-PEG-TPP were obtained in the range of 500–4000 cm^{-1}, employing a FTIR-8400S Fourier Transform Infrared Spectrometer (Shimadzu Corporation) with a resolution of 2 cm^{-1}. The ^1H NMR spectra of CPT-CA-PEG-TPP and PEG-Ce6 were recorded on an AVANCE NEO 600 NMR spectrometer (Bruker, Switzerland). The hydrated particle size of CTC micelles was measured using the 90 Plus PALS particle size analyzer (Brookhaven Instruments, USA), and the morphologies was observed under an H-7800 transmission electron microscope (TEM, Hitachi, Japan).

2.6. Physicochemical properties of polymer micelles

2.6.1. ROS responsive bond sensitive performance test

After dissolving CPT-CA in methanol, a 500 mM H_2O_2 solution was added at 37 °C for varying durations (0, 6, 24 h). At different time points, the solution was removed, the organic solvent was eliminated by rotary evaporation, and the residual solution was freeze-dried for ^1H NMR determination. Moreover, the CTC micelles were incubated with different concentrations of H_2O_2 (0 mM, 0.1 mM and 1 mM) at 37 °C for 5 days, and the morphology was observed by TEM.

2.6.2. O_2 production capacity

A portable dissolved oxygen meter was utilized to investigate the O_2 generation capacity of CTC micelles. The change in O_2 concentration was monitored over 10 min after mixing the CTC micelles at different concentrations (0, 5, 10 μg/mL, determined by the amount of CAT-loaded) with an equal concentration of H_2O_2 (1 mM). Additionally, the alteration in O_2 concentration within 10 min of the mixed solution was observed in real-time by blending the same concentration of CTC micelles (5 μg/mL, determined by the amount of CAT-loaded) with

different concentrations of H_2O_2 (0, 1, 2 mM).

2.6.3. $^1O_2$ production ability

The capability to generate $^1O_2$ was examined utilizing DPBF as a chemical probe. A defined quantity of CTC micelles was uniformly dispersed in phosphate buffered saline (PBS), to which a commensurate volume of DPBF ethanol solution was added. Prior to the application of 660 nm laser irradiation (0.1 W/cm^2), the initial absorbance of DPBF at 410 nm was ascertained through UV–vis spectroscopy, characterizing the ultraviolet profile of the mixed solution. Following this, the mixed solution, now containing CTC micelles, was exposed to a 660 nm laser for varying durations. The absorbance value of DPBF at 410 nm was then repeatedly determined using UV–vis spectroscopy, and its absorbance value change at 410 nm was observed.

2.6.4. Drug release profile

The release dynamics of CA and CPT were assessed under three distinct conditions: pH 5.0, pH 5.0 + 10 mM H_2O_2, and pH 5.0 + 10 mM H_2O_2 + Laser. At the onset of the release, the laser group underwent irradiation with a 660 nm laser at 0.5 W/cm^2 for a 5 min interval. A sample weighing 0.76 mg (CPT: 84 μg, CA: 24 μg) was positioned in a dialysis bag and subjected to agitation in a 37 °C constant-temperature shaking chamber. At predetermined time intervals (0, 0.5, 1.0, 2.0, 4.0, 6.0, 8.0, 12.0, 24.0, and 48.0 h), 400 μL of the release medium was removed and an equivalent volume was replenished. The concentrations of CPT and CA in the release solution were determined through fluorescence spectrophotometry and high-performance liquid chromatography (HPLC), respectively, culminating in the computation of the cumulative release rate for both drugs.

2.7. Cytotoxicity assays in vitro

2.7.1. Two-dimensional cell level

Lysosomes escape and Mitochondria-targeted Evaluation. 4T1 cells were seeded at a density of 2 × 10^4 cells per well in a 24-well plate, equipped with coverslips, and incubated for a period of 24 h. Following the spreading of the cells, 50 μL of CTC micelles (containing PEG-Ce6 at a concentration of 17 μg/mL) was added to each well and incubated for time intervals of 0, 2, 4, and 6 h. Subsequently, the cells were treated with the Lyso-Tracker Green and Mito Tracker Green for 20 min. Thereafter, the cells were fixed using 4 % paraformaldehyde solution for 20 min, and the nuclei were stained with DAPI for an additional 20 min. The samples were then sealed and visualized utilizing laser scanning confocal microscopy (CLSM).

Flow Cytometry to Determine Cell Uptake. 4T1 cells were seeded at a density of 4 × 10^5 cells per well in a 6-well plate and incubated for 24 h. After the spreading of the cells, an equal concentration of CLC micelles was co-incubated with the cells for varying time periods (0, 2, 4, 6 h). Following incubation, the cells were washed twice with PBS, and then treated with 1 mL of PBS to halt digestion. The cells were subsequently centrifuged to facilitate collection, washed twice with a pre-chilled solution of heparin sodium (1 mg/mL), and finally resuspended in 500 μL of PBS for the analysis of cell uptake by flow cytometry.

Biocompatibility Assessment. To appraise the biosafety of CTC micelles, normal liver LO2 cells were initially seeded in 96-well plates at a density of 5000 cells per well, followed by incubation at 37 °C and 5 % CO_2 for 24 h. Different concentrations of CTC micelles corresponding to PEG-Ce6 concentrations of 0.85, 1.7, 3.4, 8.5, and 17 μg/mL were subsequently introduced to the 96-well plate and incubated for 24 h. After the 24-h incubation, 20 μL of MTT (5 mg/mL) was added, and medium removal was removed after 4 h, 200 μL of DMSO was introduced. The absorbance value (OD) of each well was determined using a microplate reader at 570 nm, with 630 nm serving as a reference wavelength.

MTT Assay. 4T1 cells were utilized to assess the cytotoxicity of CTC micelles. The experimental groups included Control, CNC (L), TC (L), CTC, and CTC (L). 4T1 cells were seeded in 96-well plates at a density of 5000 cells per well, and varying concentrations of PBS, CNC, TC, and CTC were administered after overnight incubation to achieve PEG-Ce6 concentrations of 0.85, 1.7, 3.4, 8.5, and 17 μg/mL. Following 6 h of treatment, the CNC (L), TC (L), and CTC (L) groups were exposed to laser irradiation at 0.4 W/cm^2 for 5 min. The cytotoxicity of the polymer micelles was subsequently determined using the MTT assay after a 24 h incubation period.

Intracellular ROS Production. 4T1 cells were seeded in 24-well plates at a density of 7 × 10^4 cells per well and incubated at 37 °C and 5 % CO_2 for 24 h. The experimental groups included Control, CNC (L), TC (L), CTC, and CTC (L). The CNC (L), TC (L) and CTC (L) groups were treated for 6 h, followed by laser irradiation at 0.4 W/cm^2 for 5 min. The cells were then washed twice with PBS and incubated at 37 °C for 30 min with DCFH-DA. Then, the cells were fixed with 4 % paraformaldehyde solution for 20 min, and the nuclei were stained with DAPI for a further 20 min. The samples were subsequently sealed and visualized by CLSM.

In another experiment, 4T1 cells were seeded in 24-well plates at a density of 7 × 10^4 cells per well and incubated for 24 h. The same concentration of CTC micelles was then added and incubated for various durations (0, 6, 8, 10, 12 h). Following 6 h of treatment, all groups were subjected to laser irradiation at 0.4 W/cm^2 for 5 min. Finally, after washing with PBS, the cells were stained with DCFH-DA at 37 °C for 30 min and fixed with 4 % paraformaldehyde. The nuclei were stained with DAPI, and the green fluorescence intensity was observed using CLSM.

For the mitochondrial ROS generation experiment, 4T1 cells were treated with CTC and CNC micelles. After 6 h, followed by laser irradiation at 0.4 W/cm^2 for 5 min. Then, the cells were incubated for 30 min with Mito Tracker Red and DCFH-DA. The cell nuclei were stained with DAPI, and the overlap of green and red fluorescence was observed by CLSM.

Assay of Mitochondrial Membrane Potential (MMP). The MMP was evaluated using a JC-1 probe. 4T1 cells were seeded in 24-well plates at a density of 5 × 10^4 cells per well and incubated overnight. Different experimental groups (Control, CNC (L), TC (L), CTC, CTC (L)) were co-cultured with 4T1 cells for 12 h. The CNC (L), TC (L), and CTC (L) groups were treated for 6 h, followed by laser irradiation at 0.4 W/cm^2 for 5 min. Subsequently, mitochondria were labeled with JC-1 for 20 min, and alterations in MMP were observed using CLSM.

Dead/Live Cell (Calcein-AM/PI Double Staining) Experiment. 4T1 cells were seeded in confocal dishes and cultured for 24 h, followed by incubation with PBS, CNC (L), TC (L), CTC, and CTC (L) for 12 h (PEG-Ce6 concentration was 17 μg/mL). The CNC (L), TC (L), and CTC (L) groups were subjected to 0.4 W/cm^2 laser irradiation for 5 min after 6 h of incubation. Post-incubation, cells were washed three times with PBS, and 1.5 μL of Calcein-AM/PI was added for 15 min. After washing with PBS, 2 mL of complete medium was added, and the samples were observed with CLSM.

Apoptosis Assay. 4T1 cells were seeded at a cell density of 2 × 10^5 cells per well in 6-well plates and cultured for 24 h. After cell spreading, cells were incubated with different sample groups (Control, CNC (L), TC (L), CTC, CTC (L)) for 24 h (PEG-Ce6 concentration was 17 μg/mL). The CNC (L), TC (L), and CTC (L) groups were exposed to laser irradiation of 0.4 W/cm^2 for 5 min after 6 h of incubation. After incubation, cells were washed with PBS and digested with trypsin without EDTA. Following centrifugation washing, 400 μL of 1 × Binding Buffer was added after staining with apoptotic kit for 15 min. The percentage of apoptotic cells was then analyzed using flow cytometry.

2.7.2. Three-dimensional level

Sphere Penetration of Three-Dimensional Tumor Spheroids. Three-dimensional tumor spheres were prepared by the hanging drop method [39–41]. Initially, a 20 mg/mL agarose gel solution was heated at 80 °C and dispensed into 48-well plates (200 μL per well). After the agarose had solidified, an additional 500 μL of complete medium was added to each well. A 20 μL drop of cell suspension (3 × 10^4 cells/mL)

was placed on the lid of the 48-well culture plate to induce cell aggregation. The cells were then incubated at 37 °C and 5 % CO_2 for 72 h. Afterward, the resulting cell aggregates were transferred to the corresponding wells of the 48-well plates and cultured for an additional 24 h. Post-incubation, CTC micelles was added and incubated for different durations (0, 2, 4, 6 h), washed twice with PBS, and fixed with 4 % paraformaldehyde. The tumor spheroids were transferred to confocal dishes, and the uptake of micelles at the three-dimensional level was observed using CLSM.

Inhibition of three-dimensional tumor spheroids. The three-dimensional tumor spheroids were treated with 50 μL of materials from various groups (Control, Control (L), CNC (L), TC (L), CTC, CTC (L), with a PEG-Ce6 concentration of 17 μg/mL) over a span of 6 days. During this period, the Control (L), CNC (L), TC (L), and CTC (L) groups were exposed to laser irradiation at 0.4 W/cm^2 for 5 min following 6 h of incubation. This procedure was employed to assess the inhibitory effects of these groups on cellular proliferation. Utilizing an inverted microscope with a 10 × objective, the spheroid volume was monitored, and the long diameter (d_{max}) and short diameter (d_{min}) of each tumor spheroid were recorded. The volume was calculated using the equation $V = 0.5 \times d_{max} \times d_{min}^2$. The relative change in three-dimensional tumor spheroid volume was determined by: R=($V/V0$) × 100 %, where V is the post-treatment volume and $V0$ is the pre-treatment volume of the tumor spheroids.

Dead/Live Cell Experiment. Adhering to the aforementioned method, tumor spheres were cultivated, and the experimental groups included Control, CNC (L), TC (L), CTC, CTC (L). The CNC (L), TC (L), and CTC (L) groups were subjected to 0.4 W/cm^2 laser irradiation for 5 min post 6 h of incubation. Following 6 h of additional incubation and washed twice with PBS, 1.5 μL of Calcein-AM/PI was stained for 40 min. The samples were washed with PBS and fixed with 4 % paraformaldehyde, followed by observation via CLSM.

ROS Production. In alignment with the previously described procedure, tumor spheres were cultivated. The experimental groups comprised Control, CNC (L), TC (L), CTC, CTC (L). The CNC (L), TC (L), and CTC (L) groups underwent laser irradiation of 0.4 W/cm^2 for 5 min subsequent to 6 h of incubation. Upon completion of incubation, the samples were washed with PBS and stained with DCFH-DA at 37 °C for 30 min. After washing, the samples were fixed with 4 % paraformaldehyde, and the green fluorescence intensity was analyzed with CLSM.

2.8. ICD assay in vitro

4T1 cells were plated in 24-well plates at a density of 7 × 10^5 cells per well and cultured for 24 h. The experimental groups included Control, CNC (L), TC (L), CTC, CTC (L) (with PEG-Ce6 concentration of 17 μg/mL), and CNC (L), TC (L), and CTC (L) were exposed to 0.4 W/cm^2 laser irradiation for 5 min following 6 h of incubation. Post-irradiation, the cells were incubated for an additional 6 h, washed with PBS, fixed with 4 % paraformaldehyde for 20 min, permeated with Triton X-100 for 10 min and blocked with BSA (5 %) at room temperature for 1 h, followed by incubation with Calreticulin Rabbit Monoclonal Antibody/HMGB1 Rabbit Monoclonal Antibody at 4 °C for 12 h. After washing with PBS three times, the cells were treated with Alexa Fluor 488-labeled goat anti-rabbit IgG (H + L) for 1 h at 4 °C and stained with DAPI for 20 min. The intensity of green fluorescence was subsequently observed through CLSM.

For ATP content assay, 4T1 cells were plated in 12-well plates at a density of 2 × 10^5 cells per well and cultured for 24 h. The experimental groups included Control, CNC (L), TC (L), CTC, CTC (L) (with PEG-Ce6 concentration of 17 μg/mL), and CNC (L), TC (L), and CTC (L) were exposed to 0.4 W/cm^2 laser irradiation for 5 min following 6 h of incubation. Following incubation for an additional 6 h, the cell was collected and the intracellular released of ATP was detected by ATP assay kit in accordance with the manufacturer's protocol.

2.9. In vitro evaluation of matured DCs

Bone marrow-derived dendritic cells (BMDCs) were obtained via flushing the tibia and femur with RPMI-1640 medium containing 2 % FBS. After the removal of red blood cells (RBCs) using RBC lysis buffer, the cells were collected and cultured in RPMI-1640 medium containing 15 % FBS and 20 ng/mL GM-CSF and IL-4 for 5 days to acquire immature DCs. 4T1 cells and DCs were seeded in the upper and lower chambers of transwell plates, respectively. First, 4T1 cells were incubated with PBS, CNC (L), TC (L), CTC, CTC (L). After 12 h, the CNC (L), TC (L), and CTC (L) groups were exposed to laser irradiation at 0.4 W/cm^2 for 5 min. After laser irradiation, 4T1 cells and DCs were co-cultured for 24 h, and then the DCs were collected. The collected DCs were stained using FITC-CD86, PE-CD80. The stained DCs were washed with PBS to remove free antibodies and then analyzed by flow cytometer.

2.10. Anti-tumor efficacy assays in vivo

Biodistribution of CTC Micelles. Female BALB/c mice (aged 4–5 weeks, weighing 18–20 g) were acquired from Sipeifu (Beijing) Biotechnology Co., Ltd. All procedures related to animal handling were performed in strict compliance with the guidelines set forth by the Hebei Provincial Laboratory Animal Care and Use Committee, and the methodology was sanctioned by the Animal Experiment Ethics Committee of Hebei Medical University. Cultured 4T1 cells were concentrated and suspended in PBS to achieve a cell density of 1 × 10^7 cells/mL. A suspension of 100 μL containing 4T1 cells in PBS was injected subcutaneously into the mouse's right hindlimb. Upon the tumor reaching a volume of 150 mm^3, 200 μL of CTC micelles were administered via tail vein injection. In vivo fluorescence images of CTC micelles were captured at various time intervals (1, 6, 12, 36, 50 h) utilizing an in vivo imaging system. Following 50 h post-injection, mice were euthanized, and the principal organs (including heart, liver, spleen, lung, kidney) along with tumor tissues were collected for fluorescence imaging (Excitation wavelength: 640 nm, Emission wavelength: 700 nm).

Experimental Grouping and Administration Regimen. A 4T1 tumor-bearing mouse model was constructed according to the above method. Experimental groups and the dosing protocol were as follows: Upon the tumor volume reached approximately 80–100 mm^3, 24 tumor-bearing mice were arbitrarily segregated into 6 groups: Control, Control (L), CNC (L), TC (L), CTC, CTC (L). Treatment consisted of 100 μL injections administered via the tail vein every other day. Additionally, all laser-treated groups were subjected to 0.4 W/cm^2 laser irradiation for a duration of 5 min, 36 h subsequent to administration. The body weight and tumor volumes of the mice were monitored and catalogued on a daily basis. The tumor volume was ascertained employing the formula below:

$$Tumor\ volume\left(mm^3\right) = \left(l \times W^2\right) / 2$$

where L is the tumor length and W is the tumor width.

Upon completion of the treatment regimen, a single mouse was randomly selected from each experimental group. Tumor tissue and major organs, encompassing the heart, lung, liver, spleen, and kidney, were excised and subsequently prepared for histological examination. The specimens were fixed with 4 % paraformaldehyde and stained with hematoxylin and eosin (H&E). Histological characteristics were scrutinized under light microscopy.

Ki67 Staining. Ki67 immunohistochemical staining was performed at the treatment's conclusion to evaluate the proliferation of tumor cells across the different groups. Following the sacrifice of the mice, tumor tissues were sectioned and subjected to Ki67 labeling. These sections were then examined under light microscopy, and corresponding images were captured.

TUNEL Staining. Terminal deoxynucleotidyl transferase dUTP nick end labeling (TUNEL) staining was employed at the termination of

treatment to assess apoptosis in tumor cells across the various experimental conditions. After euthanasia, tumor tissues were subjected to TUNEL staining to mark apoptotic cells. Nuclear staining was achieved using DAPI. The stained sections were visualized via CLSM, with green fluorescence indicative of apoptotic cells. Corresponding images were acquired.

ROS Assay. The assay utilized dihydroethidium (DHE) as a ROS probe to validate the production of ROS in vivo. BALB/c mice were classified into groups (Control, Control (L), CNC (L), TC (L), CTC, CTC (L)), based on tumor size, approximately 200 mm^3 and treatment was administered via tail vein injection. Following a period of 36 h, the laser groups were subjected to laser irradiation at 0.4 W/cm^2 for a duration of 5 min. The tumors were subsequently harvested, rinsed, flash-frozen, and sectioned. The stained sections were then observed through CLSM.

2.11. In vivo ICD evaluation

CRT and HMGB1 Staining. Upon the conclusion of treatment, mice were sacrificed and tumor tissues were collected and fixed with 4 % paraformaldehyde. Fixed sections of tumor tissues were stained with primary antibodies (Calreticulin Rabbit Monoclonal Antibody/HMGB1 Rabbit Monoclonal Antibody) and secondary antibody (Alexa Fluor 488 labeled goat anti-rabbit IgG (H + L)). Nuclear staining was performed using DAPI and the samples were examined through CLSM, with green fluorescence indicating CRT and HMGB1. Images were subsequently acquired.

Detection of ATP: Upon the conclusion of treatment, mice were sacrificed and tumor tissues were collected. The ATP levels of tumors were evaluated by ATP Assay Kit.

2.12. Analysis of immune cells

CD8 Staining. For the purpose of CD8 detection, mice were euthanized at the termination of treatment, tumor tissues were harvested, fixed, and sections were prepared for CD8 immunofluorescence staining. The nuclei were stained with DAPI and the sections were viewed by CLSM. Green fluorescence denoted the presence of $CD8^+$ T cells and corresponding images were captured.

After treatment, the tumors and spleens were collected and were made into a single cell suspension. For the analysis of $CD4^+$ and $CD8^+$ T cells, tumor and spleen cells were stained with anti-CD3-PerCP, anti-CD4-FITC and anti-CD8-PE according to the manufacturer's protocols. For the analysis of T regulatory cells (Tregs), spleen cells were stained with anti-CD4-FITC, anti-CD25-PerCP and anti-FOXP3-PE according to the manufacturer's protocol.

2.13. Abscopal effect of the bilateral tumor model

4T1 cells suspension (1×10^6 cells) was injected subcutaneously into the mouse's right hindlimb (the primary tumor), and 4T1 cells suspension (5×10^5 cells) was injected subcutaneously into the same mouse left hindlimb (the distant tumor) on day 6. Upon the primary tumor volume reached approximately 80–100 mm^3, the tumor-bearing mice were randomly divided into 3 groups: Control, CTC, CTC (L). CTC micelles were injected via the tail vein every other day. Additionally, CTC (L) group was subjected to 0.4 W/cm^2 laser irradiation for a duration of 5 min, 36 h subsequent to administration. Tumor volumes of both the primary tumor and the distant tumor were measured every day.

2.14. In vivo transcriptomic analysis

4T1 tumor-bearing mouse model was constructed according to the above method. When the tumor volume reached about 200 mm^3, the tumor-bearing mice were divided into two groups and were injected intravenously with PBS and CTC (L) every other day. The tumors were collected on the 7th day, quickly frozen with liquid nitrogen, and then analyzed by high-throughput sequencing.

2.15. Biosafety evaluation

Hemolysis Rate Determination. Fresh blood was obtained from the SD rats, and RBCs were centrifuged at 3500 rpm for 15 min. Following five PBS washes, the RBCs were dispersed into 20-fold volume PBS. Different concentrations of CTC micelles were mixed with 800 μL of RBC solution, using PBS as a negative control and deionized water as a positive control. After incubation at 37 °C for 30 min and subsequent centrifugation, the absorbance value at 570 nm was determined, and the hemolysis rate was computed utilizing the subsequent formula:

$$\text{Hemolysis rate} = \frac{\text{Abs (Sample)-Abs (Negative control)}}{\text{Abs (Positive control)-Abs (Negative control)}} \times 100\%$$

Hematological Parameters and Biochemical Indices. For comprehensive in vivo safety assessment, mice were subjected to analogous treatment regimens (n = 3) as designated for the control group and CTC (L) group within the antitumor experiment. On day 14, blood samples were collected, and typical hematological markers such as white blood cells (WBC), red blood cells (RBCs), hemoglobin (HGB), hematocrit (HCT), mean red blood cell volume (MCV), mean red blood cell hemoglobin (MCH), platelets (PLT), and mean platelet volume (MPV) were assessed. An automatic analyzer was used to detection serum biochemical indices including alanine aminotransferase (ALT), alkaline phosphatase (ALP), aspartate aminotransferase (AST), urea nitrogen (BUN), and creatinine (CRE).

2.16. Statistical analysis

Statistical evaluation was performed on data represented as mean ± standard deviation. Significance levels were denoted as follows: $*p < 0.05$, $**p < 0.01$, and $***p < 0.001$, with these values indicating statistical significance.

3. Results and discussion

3.1. Characterizations and physicochemical properties

The synthetic pathways for CPT-CA-PEG-TPP and PEG-Ce6 were delineated in Scheme S1A and S1B. Initially, ROS-responsive bonds (TK and TA) were synthesized as detailed in prior literature [36,42], succeeded by the reaction of TK bonds with CPT to yield CPT-TK. Subsequently, CPT-TK reacted with TA-CA to produce CPT-CA, a process validated by ^1H NMR and MS (Figs. S1–S3). In the second stage, the mitochondria-targeted group (TPP) was conjugated with COOH--PEG_{5000}-NH_2 through amidation reaction, resulting in PEG-TPP. The subsequent emergence of a new infrared peak at 1634 cm^{-1} in the infrared spectrum of PEG-TPP, attributed to the appearance of amide band I (C═O stretching), substantiated the successful formation of PEG-TPP. ^1H NMR spectra and UV–vis absorption results provided additional evidence of this result (Figs. S4A–B). Ultimately, CPT-CA-PEG-TPP was synthesized through esterification of CPT-CA and PEG-TPP. As demonstrated in Fig. 1A, the C═O vibration of CPT-CA-PEG-TPP shifted from 1736 cm^{-1} to 1734 cm^{-1} relative to CPT-CA alone, with an intensified peak at 1734 cm^{-1}. Fig. 1B reveals that peaks at 7.60–7.93 ppm correspond to TPP's aromatic hydrogen, while peaks between 7.20 and 7.50 ppm correspond to CA's aromatic hydrogen. Additionally, the peaks of CPT aromatic hydrogen (d, e, f) and methyl hydrogen (a, b) on the TK bond were discernible. These observations collectively confirmed the successful synthesis of CPT-CA-PEG-TPP. Concurrently, PEG-Ce6 was synthesized through amidation reaction, as evidenced by a contraction vibration peak of C═O at 1632 cm^{-1} [43], indicating successful conjugation of Ce6 with PEG (Fig. 1A). ^1H NMR spectrum showing peaks (d) for carboxyl

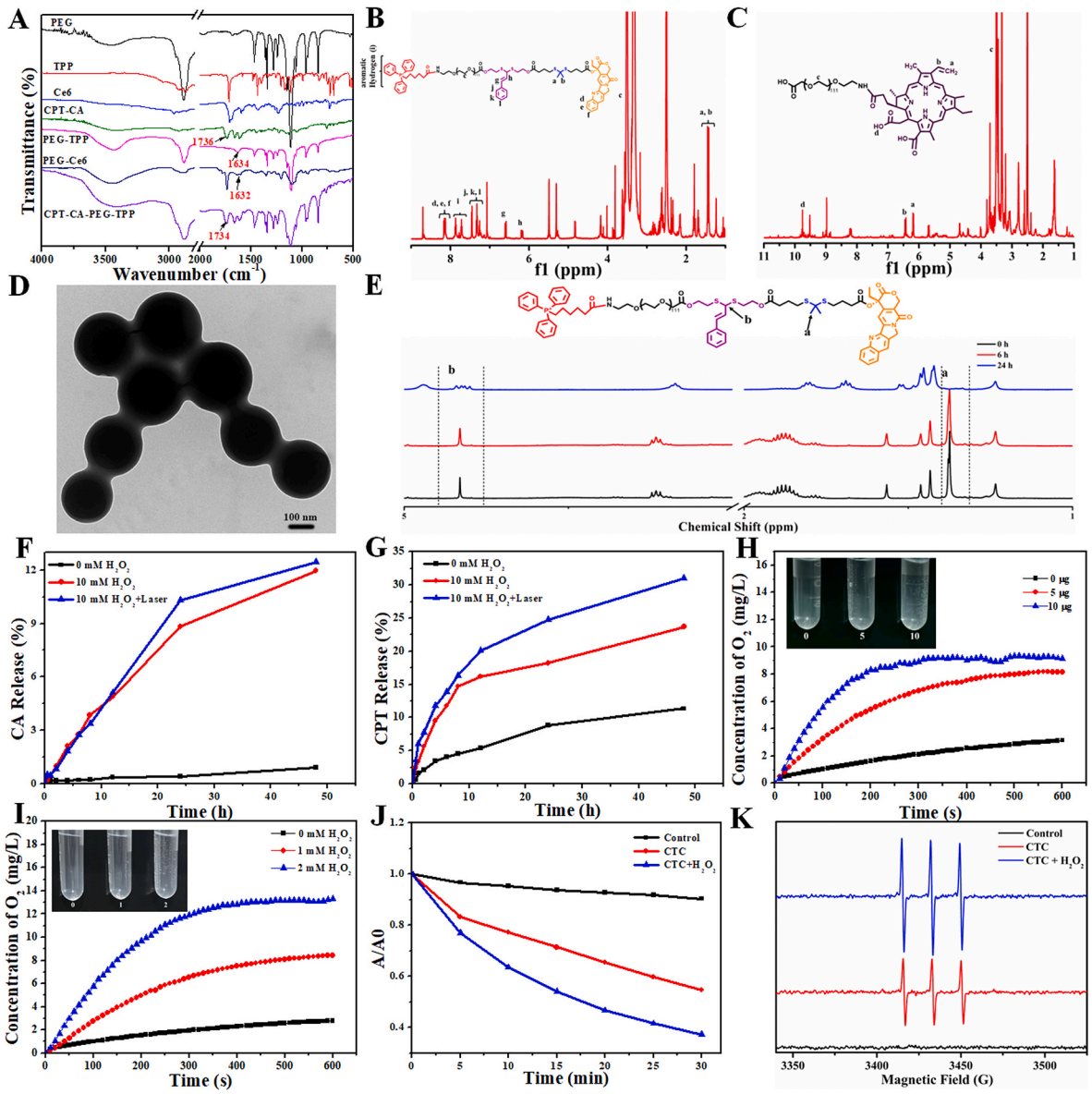

Fig. 1. (A) FTIR spectra of PEG, TPP, Ce6, PEG-TPP, CPT-CA, PEG-Ce6, and CPT-CA-PEG-TPP. (B) ^{1}H NMR spectrum of CPT-CA-PEG-TPP. (C) ^{1}H NMR spectrum of PEG-Ce6 in DMSO-d_6. (D) TEM image of CTC micelles. (E) ^{1}H NMR spectra of CPT-CA following exposure to H_2O_2 over different durations. (F) CA release and (G) CPT release under various conditions in vitro. (H) O_2 generation of CTC micelles incorporating different H_2O_2 concentrations. (I) O_2 concentration variations in H_2O_2 solution (1 mM) with the incorporation of different CTC micelles concentrations (CAT: 5/10 μg/mL). (J) The photodynamic activity and (K) ESR spectra of $^1O_2$ trapped by TEMP of CTC micelles in/without H_2O_2 after varied durations of irradiation (660 nm, 0.1 W/cm^2).

hydrogen as well as peaks (a) for imino hydrogen, further reinforced the successful synthesis of PEG-Ce6 (Fig. 1C), along with UV–vis spectra findings (Fig. S4C).

An exploration of the effects of CPT-CA-PEG-TPP and PEG-Ce6 on particle size and morphology, as influenced by varying mass ratios, followed. As displayed in Fig. S5, TEM images revealed that the mass ratio of 1.5:1 of CPT-CA-PEG-TPP and PEG-Ce6 through the ethanol injection preparation micelles yielded more uniform size. Accordingly, this ratio was selected for subsequent micelles preparation. During the self-assembly process involving CPT-CA-PEG-TPP and PEG-Ce6, CAT was encapsulated within the micelles, culminating in the formation of CTC micelles. TEM image affirmed that the CTC micelles were roughly spherical and approximately 200 nm in size (Fig. 1D). Furthermore, to evaluate the stability of the CTC micelles, hydration particle size, PDI and Zeta potential were monitored over a 7-day period using a particle size analyzer. As illustrated in Fig. S6, negligible variation in hydration particle size and Zeta potential were observed, the PDI was less than 0.2, indicating that the prepared CTC micelles have good dispersibility and stability. Thereby attesting to the CTC micelles' excellent stability.

3.2. Evaluation of ROS-responsive ability and drug release profile

The assessment of the responsiveness of CTC micelles to ROS involved an examination of the structural alterations of CPT-CA subsequent to incubation with identical concentration of H_2O_2 over various time frames within a methanol solution, as analyzed by ^{1}H NMR. As depicted in Fig. 1E, the positions labeled as a and b peaks pertain to ROS-responsive TK and TA bonds, which undergo cleavage in the presence of H_2O_2, culminating in a reduction or even disappearance of NMR peaks. It is discernible from Fig. 1E that following 6 h incubation of CPT-CA with H_2O_2, the NMR peak intensity at the a and b positions diminishes, and upon further extension of the incubation time with H_2O_2 to 24 h, the corresponding NMR peaks vanish, thereby substantiating that the synthesized CPT-CA exhibits ROS responsiveness. Subsequently,

the study probed the lysis of CTC micelles after a 5-day incubation with varying concentrations of H_2O_2 (0, 0.1, 1 mM) utilizing TEM. As illustrated in Fig. S7, post-incubation for 5 days with 0 mM H_2O_2, the CTC micelles maintained their original morphology, while a progressive increase in H_2O_2 concentration elicited a commensurate augmentation in the lysis degree of CTC micelles. When the CTC micelles were subjected to 1 mM H_2O_2 for a span of 5 days, pronounced morphological alterations ensued, accompanied by the most substantial lysis. In addition, TEM image show that the structure of CTC micelles also collapsed significantly when the concentration of H_2O_2 was 0.1 mM, which laid the foundation for the responsive cracking of nanomicelles into the tumor microenvironment. These findings corroborate the ROS-responsive nature of CTC micelles.

The evaluation of the drug release properties of CA and CPT necessitated an exploration of the release dynamics at 37 °C, under distinct H_2O_2 concentration, and with or without laser irradiation. Fig. 1F and G reveal that CTC micelles manifested negligible CA and CPT release at 0 mM H_2O_2, in contrast to a notable enhancement in drug release at 10 mM H_2O_2, yielding CA and CPT releases of 11.9 % and 23.6 %, respectively, at the 48-h mark. Additionally, before the release beginning, apply laser irradiation of 0.5 W/cm^2 for 5 min to trigger an increment in the release quantities of CA and CPT, with release percentages of 12.4 % and 31.0 %, respectively, at 48 h. This phenomenon can be attributed to Ce6, functioning as a photosensitizer, which generates ROS upon laser irradiation at 660 nm [44], thereby inducing a higher release of CA and CPT. These outcomes delineate that the H_2O_2 concentration and laser irradiation significantly influence the release of CA and CPT.

3.3. O_2 production and $^1O_2$ capacity assessment

The encapsulation efficiency of CAT within the CTC micelles was determined to be 13 % using the BCA method. The ability to generate O_2 within the micelles was assessed by employing a portable dissolved oxygen meter to observe the O_2 production. Fig. 1H and I illustrates that CTC micelles, as anticipated, demonstrated catalase-dependent catalytic activity with respect to H_2O_2. That is, the rate of O_2 production progressively increased in accordance with the augmentation of CAT content in the micelles. Moreover, the O_2 production capacity of CTC micelles exhibited a positive correlation with the concentration of H_2O_2; specifically, an increase in H_2O_2 concentration led to a gradual enhancement in the rate of O_2 production when the concentration of CTC micelles remained constant.

Further evaluation was conducted to understand the in vitro photodynamic characteristics of CTC micelles, particularly focusing on its $^1O_2$ generation capacity. This was accomplished by monitoring changes in the absorbance value of 1, 3-diphenylisobenzofuran (DPBF) at a wavelength of 410 nm. As depicted in Fig. 1J, the absorption intensity of DPBF remained largely unchanged following 30 min of irradiation with a 660 nm laser at a power density of 0.1 W/cm^2, thus indicating commendable photostability of DPBF. Conversely, the presence of CTC micelles prompted a substantial decrease in the absorbance value of DPBF at 410 nm, with the decline intensifying in conjunction with prolonged illumination (Fig. 1J). These observations affirm that CTC micelles possess a robust $^1O_2$ generation capacity. Furthermore, when the concentration of CTC micelles was maintained, the absorbance value of DPBF at 410 nm exhibited a more marked reduction in the presence of H_2O_2 (1 mM) compared to its absence (Fig. S8). This underscores the likelihood that the enhanced photodynamic activity is attributable to O_2 production, facilitated by the decomposition of H_2O_2, a reaction catalyzed by the micelle-encapsulated CAT. In addition, the $^1O_2$ production of CTC micelles in the presence of H_2O_2 by electron spin resonance (ESR) measurement. CTC micelles show a characteristic 1:1:1 triplet ESR signal under 660 nm laser irradiation when 2,2,6,6-tetramethylpiperidine (TEMP) as a spin-trapping reagent (Fig. 1K), which is assigned to the signal of TEMP-$^1O_2$ produced through the reaction of $^1O_2$ and TEMP under experimental conditions. Considering the effective H_2O_2 catalytic ability, we measured the $^1O_2$ generation ability of CTC micelles at a mimetic H_2O_2 environment. The ESR signals was intensified in the presence of H_2O_2 suggesting that CTC micelles can utilize H_2O_2 to produce $^1O_2$. This outcome mirrors the result shown in Fig. 1J. Based on all above analyses, we concluded that CTC micelles have a good ability to generate $^1O_2$. DPBF and ESR results showed that CTC micelles was activated by 660 nm laser irradiation and produced large amounts of $^1O_2$, and CAT could further catalyze H_2O_2 to produce O_2, resulting in increased $^1O_2$ generation. Thereby, laser irradiation and CAT were crucial domino causing a whole row of latter dominos to fall inducing a domino effect for tumor therapy.

3.4. Cellular assays in vitro

3.4.1. In vitro cellular assays at two-dimensional level

Lysosomes escape. To achieve mitochondrial targeting, effective lysosomes escape is essential for internalized micelles. Lysosomes escape of CTC micelles within the 4T1 cells were monitored in real-time by CLSM. 4T1 cells nuclei and lysosomes were stained by DAPI and LysoTracker Green, respectively. As depicted in Fig. S9, the red fluorescence from CTC micelles matched well with green fluorescence and displayed yellow color after treated with 4T1 cells for 2 h. However, as the incubation time was extended, the overlap between the red and the green fluorescence became decreased. This decrease in co-localization was evident from the decrease in Pearson's correlation coefficient (Rr) from 0.78 to 0.77, which further decreased to 0.67. This result demonstrates that CTC micelles can effectively escape from lysosomes. Moreover, Zheng and co-workers reported that such effectively lysosomal escape of nanosystem is probably a result of the good lipophilicity of the TPP targeting ligand [45].

Mitochondria-targeted and Cellular Uptake. The mitochondria-targeted ability of CTC micelles was assessed using CLSM. A detailed investigation was conducted into the colocalization of mitochondria following various incubation durations between CTC micelles and 4T1 cells. The 4T1 cells were incubated with CTC micelles for time periods of 0 h, 2 h, 4 h, and 6 h, and subsequently stained with DAPI and Mito-Tracker (a commercial mitochondrial green dye). Fig. 2A reveals that, compared to 0 h incubation, a minimal number of micelles reached the mitochondria after 2 h of co-incubation with 4T1 cells. However, as the incubation time was extended, the micelles penetrating the cells gradually increased. Upon 6 h co-incubation with 4T1 cells, CTC micelles (Ce6: red fluorescence) and Mito-Tracker exhibited significant overlap within 4T1 cells, manifesting as bright yellow fluorescence. This evidence substantiates the exceptional mitochondria-targeted ability of CTC micelles. To present the mitochondrial colocalization effect more intuitively at different time intervals, the overlap degree of green and red fluorescence at distinct time was further analyzed using Image J software. The analysis elucidated that the concurrence of green and red fluorescence progressively intensified with the extension of time. Fig. S10 illustrates that, compared to 0 h, the intracellular fluorescence intensity escalated incrementally with prolonged incubation, confirming that the internalization of CTC micelles into the cells gradually augmented. After a 6 h incubation with 4T1 cells, a pronouncedly higher fluorescence intensity was observed, indicating that CTC micelles could be effectively endocytosed into tumor cells.

Cytotoxicity. The mitochondria-targeted and cellular uptake results ascertain that CTC micelles were effectively internalized by 4T1 cells and exhibit superior mitochondria-targeted capabilities, laying the groundwork for their potential tumor treatment effects. To probe the synergistic therapeutic implications of CTC system-mediated mitochondrial targeting, combined with enhanced chemotherapy and PDT, cytotoxicity was appraised in different groups post 24 h co-incubation with 4T1 cells using the MTT method. Fig. 2B illustrates that the CTC group's cell viability rate was 52 %, markedly greater than that in the CTC (L) group (5 %). This result suggests that the administration of 660

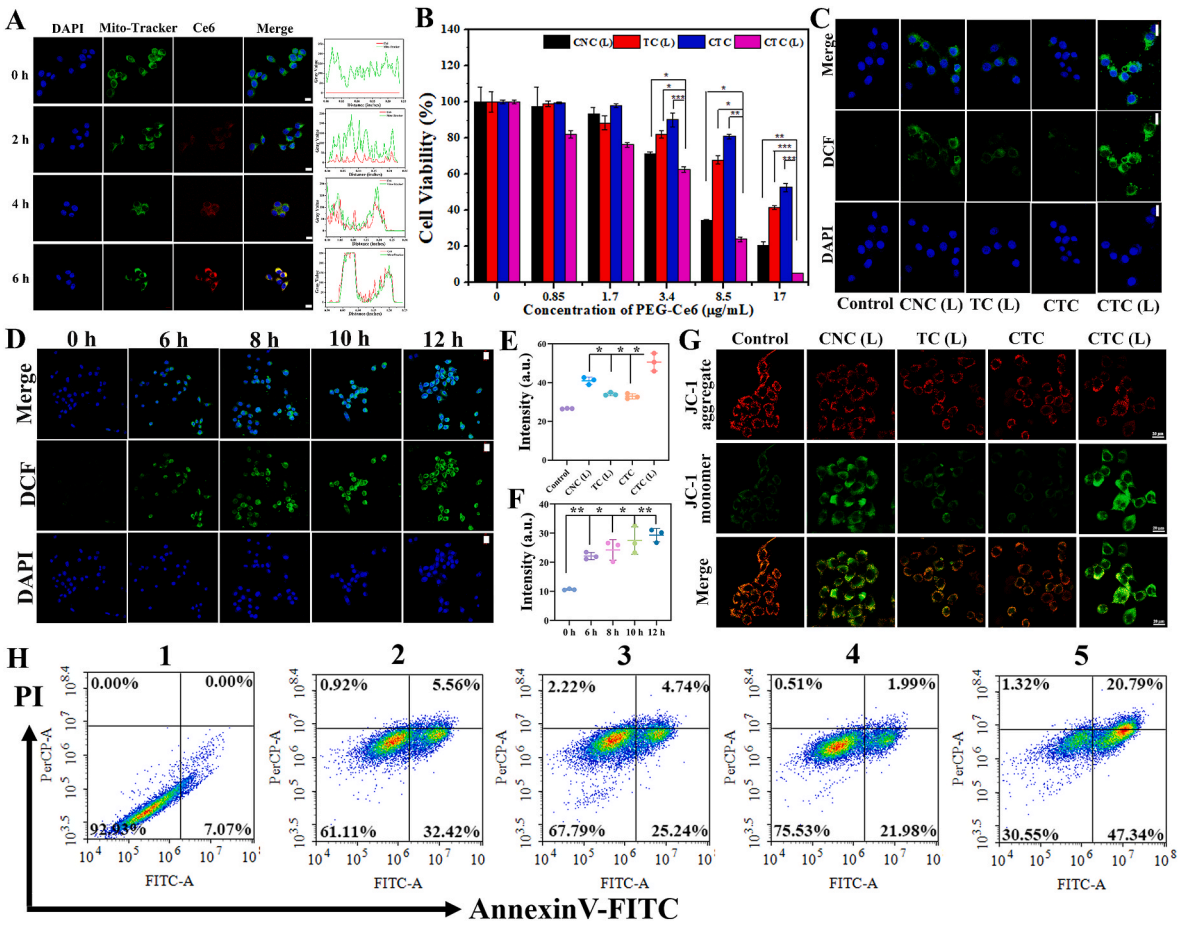

Fig. 2. (A) Mitochondrial co-localization of CTC micelles in 4T1 cells. (B) Analysis of viability of 4T1 cells subjected to various treatments at 37 °C over a 24-h period. CLSM images of (C) intracellular ROS generation in 4T1 cells subjected to diverse treatments, utilizing DCFH-DA as the probe, and (D) ROS generation following treatment with CTC micelles for varied durations and laser irradiation post 6-h co-incubation. (C) and (D) represent mean fluorescence intensity analyses with Image J, corresponding to (E) and (F) (n = 3), respectively. (G) CLSM images of JC-1 stained 4T1 cells following distinct treatments. (H) Flow cytometric examination of 4T1 cells apoptosis following exposure to different treatments. Where: (1) Control, (2) CNC (L), (3) TC (L), (4) CTC, (5) CTC (L). $*p < 0.05$ and $**p < 0.01$. scale bar = 20 μm.

nm laser irradiation can instigate cells to generate more ROS, thereby stimulating more drug release and facilitating a more potent cell-killing effect. The cell survival rate of TC (L) group was significantly elevated compared to the CTC (L) group, which implies that CAT within CTC micelles, upon targeting mitochondria, can catalyze H_2O_2 to produce O_2, thus achieving enhanced PDT. Additionally, the CNC (L) group also displayed a higher cell survival rate compared to the CTC (L) group, as CTC micelles target mitochondria to accomplish enhanced PDT, thereby inducing more robust oxidative stress in the mitochondria and consequent increased apoptosis. To more vividly represent the cytotoxicity of the CTC micelles, live/dead cell staining experiment was employed, with live cells stained green by Calcein-AM and dead cells stained red by Propidium Iodide (PI) [46]. Fig. S11 shows almost no cell death in the control group, while the CNC (L), TC (L), CTC, and CTC (L) groups exhibited varying degrees of cell death, with the CTC (L) group showing the most potent red fluorescence and the weakest green fluorescence, corroborating that CTC (L) could induce greater cell death. The staining outcome align with the MTT result, collectively affirming that CTC (L) micelles target mitochondria to realize enhanced chemotherapy and PDT, resulting in the most substantial cytotoxicity.

Intracellular ROS Production. Continuous and adequate intracellular ROS production stands as a fundamental requisite for the induction of pronounced oxidative stress within the mitochondria, and consequently, the onset of ICD. Accordingly, to evaluate the generation of intracellular ROS following the co-incubation of 4T1 cells with various material groups, intracellular ROS was marked by the ROS fluorescent probe (DCFH-DA). The staining principle entails that once DCFH-DA permeates the cellular membrane, it is deacetylated by intracellular esterase to form non-fluorescent DCFH, which can be oxidized by ROS to emit green fluorescence [47], detectable via CLSM. As depicted in Fig. 2C, the CTC group can prompt cells to yield a modest quantity of ROS compared to the control group, demonstrating that mitochondrial endogenous ROS as the beginning of the domino effect led to the cleavage of some ROS-responsive bonds. However, subsequent to laser irradiation at 660 nm, the CTC (L) group exhibits robust green fluorescence, and the volume of ROS production is substantially augmented. Although the CNC (L) group revealed strong green fluorescence, it was diminished compared to that in the CTC (L) group, thus attesting that the micelles can stimulate cells to generate increased ROS following mitochondrial targeting. In addition, the green fluorescence of the TC (L) group remains weaker than that of CTC (L), attributable to CAT's role in catalyzing the H_2O_2 production of O_2, thereby enhancing PDT and subsequently inducing augmented ROS production. For a more intuitive representation of the fluorescence intensity variance among different groups, the mean fluorescence intensity after incubation with varying groups was further analyzed by Image J software, resulting in values of 26.6 ± 0.1, 41.1 ± 1.8, 34.2 ± 0.8, 33.0 ± 1.3, and 50.6 ± 4.6, respectively (Fig. 2E). Additionally, to explore the capability of the CTC micelles system in promoting sustained cellular ROS production, the ROS generation in cells after diverse co-incubation durations with the

CTC micelles and 4T1 cells was investigated via CLSM. It warrants noting that following a 6 h co-incubation of CTC micelles with 4T1 cells, laser irradiation is administered to effectuate PDT, inducing further ROS production. As illustrated in Fig. 2D, the findings affirm that CTC micelles can perpetually induce intracellular ROS generation post-laser irradiation, and the mean intracellular fluorescence intensity across different groups was also computed utilizing Image J (Fig. 2F). In addition, we evaluated the generation of ROS within mitochondria. After the CNC and CTC micelles were incubated with 4T1 cells for the same time, the cell nuclei, mitochondria and ROS were stained with DAPI, Mito-tracker and DCFH-DA, respectively, and the result was shown in Fig. S12. Compared with the control group, both CNC (L) and CTC (L) group can induce ROS generation in mitochondria. However, the CTC (L) group has stronger green fluorescence, and the red and green fluorescence matched well and displayed stronger yellow color, which proved that nanomicelle modification of TPP can effectively induce mitochondrial ROS generation. These results demonstrate that enhanced chemotherapy and photodynamic therapy after targeting mitochondria by CTC micelles can induce stronger ROS production through the domino effect. Moreover, these findings substantiate the underlying framework for the actualization of intracellular ICD.

Mitochondrial damage. To evaluate the extent of mitochondrial impairment inflicted upon 4T1 cells by CTC micelles, variations in the mitochondrial membrane potential (MMP) were ascertained through JC-1 staining. Under standard physiological conditions, JC-1 aggregates within the mitochondrial matrix, thereby yielding red fluorescence. However, in the event of MMP loss, the aggregated red fluorescence of JC-1 transitions to monomer green fluorescence [48]. As delineated in Fig. 2G, in comparison with the control group, the red fluorescence of the other groups decreased and green fluorescence increased, indicating that the incubation with different groups induced variable degrees damage of mitochondria, with the CTC (L) group having the greatest attenuation of red fluorescence and the strongest green fluorescence, thus signifying that CTC micelles may inflict more substantial damage to mitochondria post-mitochondrial targeting.

Apoptosis. To further validate that CTC (L) possesses an enhanced cell-killing effect, apoptosis induced by the different groups was explored using flow cytometry. Fig. 2H reveals that the apoptosis rate of the CTC group was 23.97 %, the TC (L) group's rate was 29.9 %, and the CNC (L) group's rate was 37.9 %, all of which were lower than the CTC (L) group's rate of 70 %. This evidence verifies that CTC micelles, after targeting mitochondria, brought about more potent oxidative stress, leading to augmented apoptosis by achieving enhanced chemotherapy and PDT.

3.4.2. Cytotoxicity evaluation at the three-dimensional level

Research has demonstrated that three-dimensional (3D) tumor spheroids more accurately reflect the tumor microenvironment [49,50]. Encouraged by the results produced from two-dimensional cell experiments, 3D tumor spheroids were used to understand the local

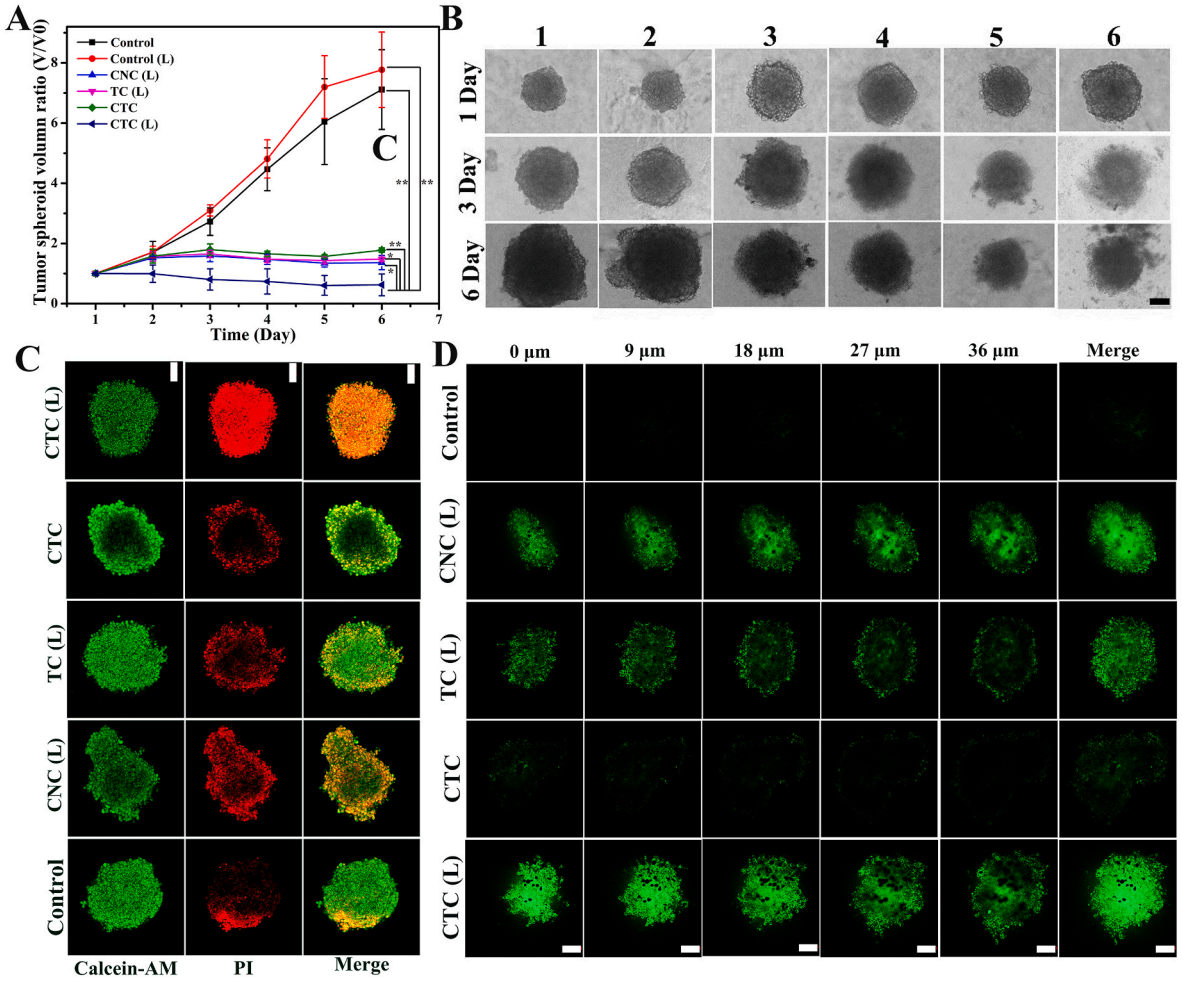

Fig. 3. (A) Relative 3D tumor spheroids volume subsequent to various treatments. (B) Representative microscopic images of 4T1 tumor spheroids with different groups. (C) CLSM images of the 3D tumor spheroids of 4T1 cells stained with Calcein-AM/PI following treatment with various groups at 24 h. (D) CLSM images of 4T1 tumor spheroids subsequent to 12 h of co-incubation with different groups, and staining with DCFH-DA. Where (1) Control, (2) Control (L), (3) CNC (L). (4) TC (L). (5) CTC. (6) CTC (L), $^{*}p < 0.05$ and $^{**}p < 0.01$. scale bar = 100 μm.

spatiotemporal effects of micelles on tumor cells in the tumor microenvironment (e.g., overexpression of H_2O_2) [51,52]. The effective internalization of micelles by tumor spheroids serves as a prerequisite for their therapeutic efficacy within tumor spheres. Initially, 3D tumor spheroids were fabricated utilizing the hanging drop method. Consequently, CTC micelles and 3D tumor spheroids were co-incubated at varying durations to explore its penetration into the 3D level. Fig. S13 illustrates that as incubation time prolongs, the red fluorescence intensity (attributed to Ce6) within the tumor spheroids progressively escalates, affirming that an increasing quantity of micelles is assimilated by the tumor sphere, corroborating the findings from the 2D uptake experiment. Subsequently, disparate groups of materials were co-incubated with the tumor spheroids for an aggregate duration of 5 days, with the growth dynamics of the tumor spheroids being continually monitored. As depicted in Fig. 3A, tumor spheroids growth in the control (L) group remained largely uninhibited relative to the control group, attesting that laser irradiation in isolation essentially did not impede the expansion of tumor spheroid. In contrast to the CNC (L), TC (L), and CTC groups, the CTC (L) group manifested the most pronounced tumor spheroid growth restraint, owing to the micelles achieving augmented PDT under laser irradiation at 660 nm subsequent to mitochondrial targeting, thereby liberating additional chemotherapeutic agents. This could provoke mitochondria to engender a more potent oxidative response and thereby induce augmented cellular death. Fig. 3B showing exemplary pictures of the tumor spheroids suppression experiment. In succession, the cytotoxicity of CTC micelles at the 3D cellular level was further substantiated by live/dead cell staining assay, as demonstrated in Fig. 3C, corroborating that CTC (L) could induce a more potent cytotoxic effect, harmonizing with the 2D level findings of live/dead cell staining.

Subsequently, DCFH-DA was employed as a ROS probe to assess ROS production in cells following the co-incubation of 3D tumor spheroids with diverse material groups. As presented in Fig. 3D, the CTC (L) group exhibited a more pronounced green fluorescence signal relative to other groups, signifying that CTC (L) can more efficaciously instigate ROS generation within 3D tumor spheroids, aligning with the ROS production observations at the 2D level. Cumulatively, these findings unequivocally affirm that the synthesized CTC micelles can execute antitumor functions in a manner more congruent with the tumor microenvironment, thereby laying a theoretical foundation for subsequent investigations into the in vivo anti-tumor efficacy of CTC micelles.

3.5. Micellar-induced ICD effect

ICD is a distinctive form of cellular demise with the capability to enhance the infiltration of immune effector cells and remodel the tumor microenvironment. Such actions are instrumental in amplifying systemic anti-tumor immunity, ultimately aiming for comprehensive tumor eradication post-treatment. ICD is delineated by the liberation of damage-associated molecular patterns (DAMPs), including the externalization of CRT on the cellular membrane surface, the excretion of high-mobility group box 1 (HMGB1) proteins and the secrete of adenosine triphosphate (ATP) [53]. These DAMPs send out signals of “find me” and “eat me” to catalyze the migration and maturation of DC, subsequently leading to antigen presentation to T cells and culminating in the recruitment of cytotoxic T lymphocytes (CTLs) into the tumors to achieve a tumor-killing immune response [54,55], hence positioning ICDs as pivotal catalysts for immune engagement.

In a quest to ascertain whether sustained ROS production within cells can efficaciously instigate ICD, the expression of CRT on the cellular membrane, along with the discharge of HMGB1 within cells, were appraised via immunofluorescence staining. As illustrated in Fig. 4A, the control group manifested negligible CRT expression on the cellular membrane surface. Conversely, the CNC (L), TC (L), CTC, and CTC (L)

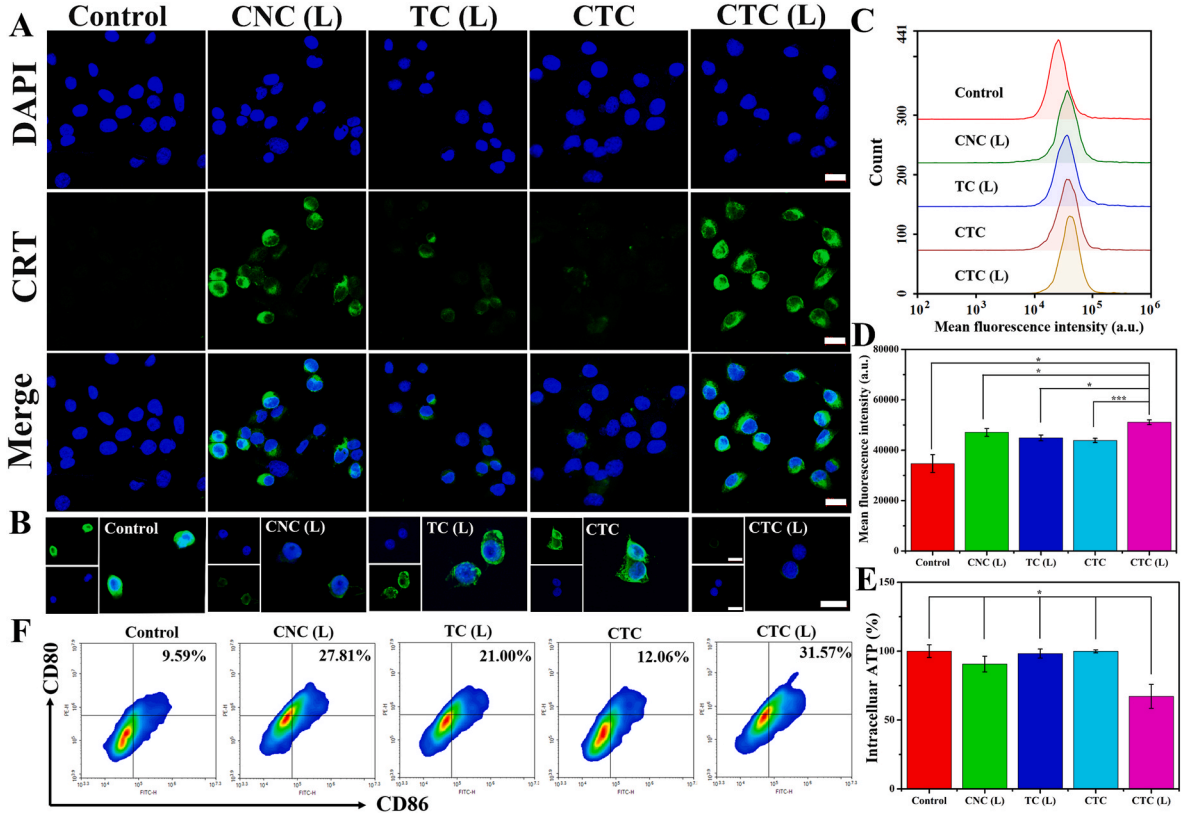

Fig. 4. CLSM images of CRT expression (A) and HMGB1 release (B) in 4T1 cells after treated with different groups. (C) Flow cytometry analysis of surface CRT exposure induced by different groups (n = 3). (D) Mean fluorescence intensity of (C). (E) ATP levels of 4T1 tumor cells treated with different groups (n = 3). (F) Flow cytometry analysis of matured DCs ($CD80^+CD86^+$) cocultured with 4T1 cells after various groups. *$p < 0.05$ and ***$p < 0.001$, scale bar = 20 μm.

groups exhibited CRT translocation on the cellular membrane surface post-co-incubation with 4T1 cells. Among these, the CTC (L) group demonstrated particularly conspicuous CRT translocation, attributable to the enhanced PDT attainable through laser irradiation subsequent to mitochondrial targeting. This consequently leads to the liberation of an augmented quantity of chemotherapeutic agents and the subsequent induction of increased ROS production, culminating in more pronounced CRT exposure. The escalation of ROS levels within tumor cells expedites the liberation of HMGB1 from the nucleus to the extracellular environment. Previous intracellular ROS generation experiments have validated that the CTC (L) group exhibits superior ROS generation prowess, which is anticipated to further enhance the dissemination of HMGB1 from the nucleus to the extracellular matrix. Fig. 4B visually corroborates that, relative to the control group, the CNC (L), TC (L), CTC and CTC (L) groups are capable of inducing HMGB1 release. Among these, the CTC (L) group distinctly augments the liberation of HMGB1 from the nucleus to the extracellular matrix. Moreover, we measured the CRT exposure rate of tumor cells after treatment with different groups by flow cytometry. As shown in Fig. 4C and D, compared to the control group, the mean fluorescence intensity of CNC (L), TC (L), CTC, and CTC (L) groups increased, indicating that different groups exhibited CRT translocation on the cellular membrane surface after coincubation with 4T1 cells. Among these, the CTC (L) group had a stronger mean fluorescence intensity, which proved that its induced CRT exposure was more obvious. This result was consistent with CLSM images. Finally, ATP secrete was monitored by an ATP detection kit. As illustrated in Fig. 4E, compared to other groups, the CTC (L) group exhibited lower intracellular ATP levels, which was consistent with the conclusions from the CRT exposure and HMGB1 release analysis. These results indicate that the constructed ROS-responsive and triple-synergistic mitochondria-targeted polymer micelles (CTC micelles) effectively induce ICD.

DCs maturation is a crucial step in initiating an immune response. To investigate this, mouse bone marrow-derived DCs (BMDCs) from BALB/c mice were co-cultured with 4T1 cells after different treatments, and the maturation of DCs was assessed using flow cytometry. As shown in Fig. 4F, the proportion of mature DCs was 9.59 % in the control group, while in the CNC (L), TC (L), and CTC groups, it was 27.81 %, 21.00 %, and 12.06 %, respectively. Notably, upon CTC (L) treatment, the proportion of mature DCs increased to 31.57 %. This suggests that the prepared CTC micelles targeting mitochondria can enhance chemotherapy and PDT under 660 nm laser irradiation can stimulate more DCs to mature, augmenting the immune response.

3.6. *In vivo anti-tumor activity*

Drawing upon the foundational in vitro studies, the in vivo investigation commenced with an exploration to ascertain the optimal duration for light exposure subsequent to administration. To this end, the

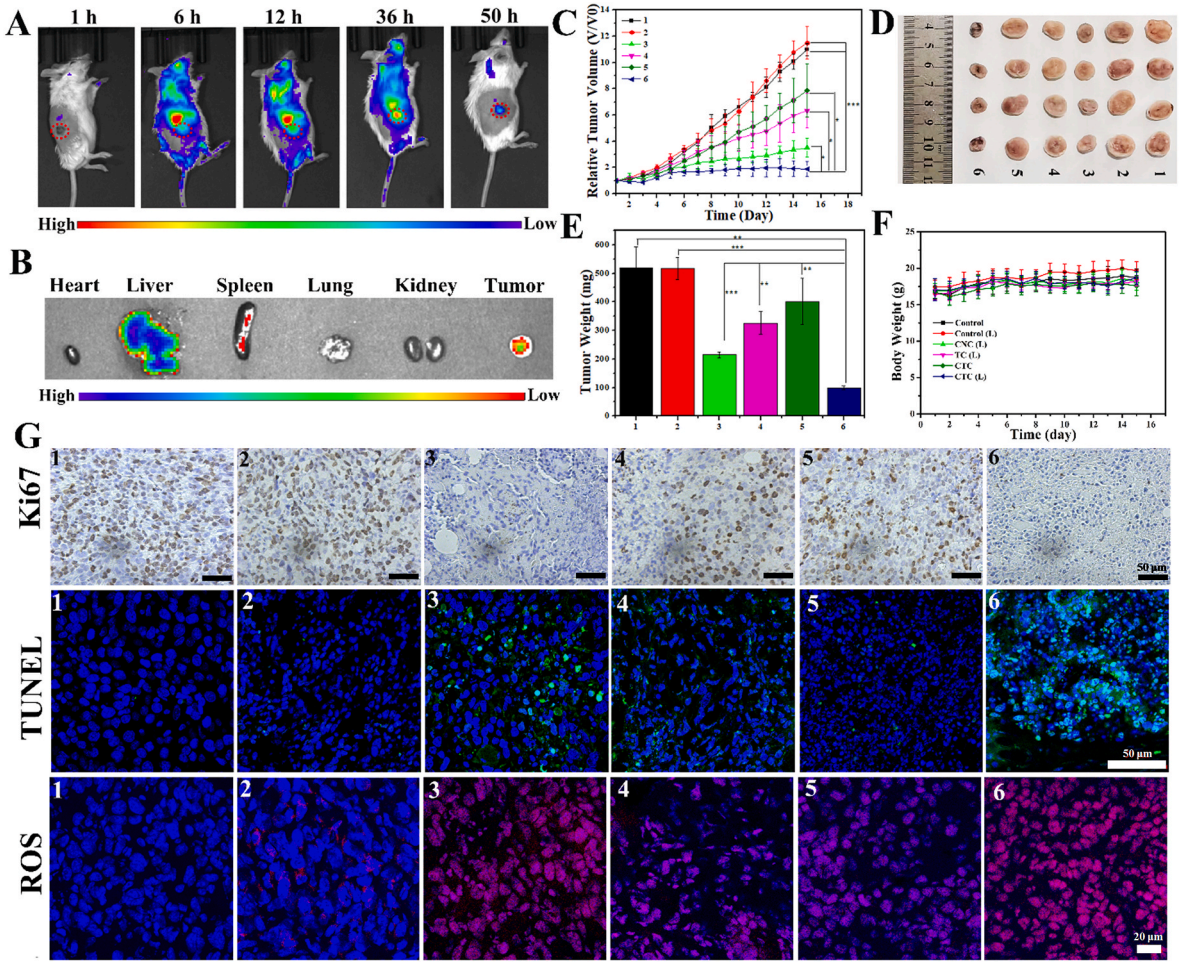

Fig. 5. (A) Fluorescence imaging of 4T1 tumor-bearing mice at differing intervals post tail vein injection of CTC micelles. (B) Fluorescence imagery of excised major organs and tumor subsequent to a 50-h post-CTC micelles injection. (C–E) Relative tumor volume, visual representation of tumors, and tumor weights across varied treatments (n = 4). (F) Evolution of body weight within the mice across the 14-day treatment regimen. (G) Ki67, TUNEL and ROS staining of tumor tissues extracted from 4T1 tumor-bearing mice at the 14th day. $^{*}p < 0.05$, $^{**}p < 0.01$ and $^{***}p < 0.001$. Where (1) Control, (2) Control (L), (3) CNC (L), (4) TC (L), (5) CTC, (6) CTC (L).

accretion of CTC micelles within 4T1-bearing mice was initially scrutinized employing an In Vivo Imaging Systems (IVIS) system. The time-dependent dispersion of CTC micelles in 4T1-bearing mice via animal fluorescence imaging was monitored, following the injection of CTC micelles through the tail vein. As depicted in Fig. 5A, the most robust fluorescence signal was discernible in the tumor region at 36 h post-tail vein injection, thereby corroborating that CTC micelles were adept at concentrating efficiently at the tumor locale within this timeframe. Conversely, a waning in fluorescence intensity at the tumor site was observable at 50 h, a phenomenon attributable to the progressive metabolism of the CTC micelles. Subsequent to tail vein injection for a period of 50 h, mice were euthanized, and the principal organs (heart, liver, spleen, lung, kidney) and tumor tissues were harvested for fluorescence imaging (Fig. 5B). The imaging outcomes revealed pronounced fluorescence within the tumor tissues, thereby testifying to the adept tumor-targeting properties of the prepared CTC micelles. Of noteworthy mention is the detection of strong fluorescent signal within liver organ, a finding indicative of CTC micelles metabolism within the body. To further assess the synergistic impact of mitochondrial-targeted CTC micelles on the amplification of in vivo chemotherapy, PDT, and immunotherapy, BALB/c mice were specifically chosen for a comprehensive study of the anti-tumor efficacy of CTC micelles in vivo. 4T1 tumor-bearing mice model was constructed and upon the tumor volume expanding to approximately 80–100 mm^3, the mice were arbitrarily allocated into 6 cohorts for administration via tail vein injection. Subsequently, the tumor volume of the mice was meticulously measured on a daily basis (Fig. 5C). At the conclusion of the 14-day treatment period, the excised tumor tissues from the varying groups were assembled and weighed (Fig. 5D and E). Fig. 5C illustrates that the control and control (L) groups exerted no inhibitory influence on tumor proliferation, thereby affirming that laser irradiation in isolation did not manifest therapeutic effects on tumor growth. Conversely, when contrasted with the control group, the remaining groups manifested disparate degrees of tumor growth inhibition. Notably, the tumors of CTC (L) group were obvious smaller in size and weight than other groups (Fig. 5D and E), indicating the tumor suppressor impact most conspicuous. These findings collectively substantiate that CTC micelles, upon targeting mitochondria, engender augmented PDT, thus facilitating increased drug liberation, stimulating the tumors to generate augmented ROS, inducing a more potent ICD effect, and culminating in a pronounced tumor suppressor effect. Furthermore, a continuous monitoring of weight variations in mice across diverse treatment groups over the 14-day period, as portrayed in Fig. 5F, revealed no substantial fluctuations in body weight among the different groups during the treatment course. This observation underscores the satisfactory biocompatibility of CTC micelles.

To augment the understanding of the tumor treatment efficacy of CTC micelles, tumor tissues were collected post-sacrifice of mice and subjected to staining with H&E, Ki67, and TUNEL. As delineated in Fig. 5G and S14, the H&E staining results reveal that regions of necrosis or apoptosis were identifiable in tumor sections following 14 days of treatment across various groups when contrasted with the control and control (L) groups (Fig. S14). The CTC (L) group, in particular, exhibited an expansive area of necrosis or apoptosis within tumor sections, thereby signaling a superior anti-tumor effect in comparison with other groups. Ki67, functioning as a marker of cell proliferation, is often employed in the evaluation of tumor therapeutic effects. Thus, Ki67 (brown) immunohistochemical staining was conducted on tumor tissues subjected to treatment by diverse groups. The comparative analysis with control and control (L) groups elucidates that the expression of Ki67 in tumor tissues witnessed a reduction post-treatment with other groups, with the expression within tumor tissues of the CTC (L) group being markedly discernible. This underscores the notion that the CTC (L) group possesses the capability to augment therapeutic effects through the inhibition of 4T1 tumor cells' proliferation. Furthermore, the results of TUNEL staining allow for the observation that the CTC (L) group exhibited a significantly larger area of tumor cell apoptosis (green) as opposed to other groups. This substantiates that CTC (L) group can achieve enhanced PDT following mitochondrial targeting, thereby fostering increased drug release and subsequent promotion of more ROS production within tumor tissues. This leads to the induction of more robust ICD effects, thereby manifesting more potent tumoricidal effects.

In a bid to gauge the ROS level within tumor tissues, subsequent to a 36 h injection of varied material groups into the tail vein, the tumor tissues were harvested and sectioned. The nuclei and ROS of 4T1 cells were stained with DAPI (blue) and DHE (red), correspondingly, with the results depicted in Fig. 5G. Relative to the control and control (L) groups, the CTC group exhibited weak red fluorescence, thereby affirming that CTC can stimulate the tumor tissue to engender a minimal amount of ROS. However, upon the administration of 660 nm laser irradiation, ROS generation experienced a substantial increase, highlighting that enhanced PDT can be actualized under laser irradiation, which subsequently triggers more drug release and thus mediates elevated ROS production. Additionally, the red fluorescence within the CNC (L) group was found to be feebler than that in the CTC (L) group, indicating that a more robust oxidative stress could be induced to generate increased ROS following mitochondrial targeting. This is in alignment with the outcomes of ROS production at the cellular stratum. Such results signify that CTC (L) can efficaciously instigate ROS production in vivo, thus laying the groundwork for the in vivo manifestation of ICD.

3.7. Immune activation in vivo

We constructed polymer micelles can stimulate sustained, stable, and sufficient ROS production in cancer cells, inducing an effective ICD. Thereby fosters the phagocytosis and presentation of tumor antigens by dendritic cells, further efficiently initiating specific anti-tumor immune responses (Fig. 6A). Given the exceptional in vivo ROS generation capacity of polymer micelles, an investigation was initiated to assess the capability of CTC micelles to instigate ICD in vivo. Specifically, the exposure of CRT at tumor locales and the discharge of HMGB1 were analyzed by means of immunofluorescent staining subsequent to treatment. As elucidated in Fig. 6B, the CRT staining outcomes indicate an almost negligible expression of CRT within the control and control (L) groups. Conversely, CRT exposure is discernible within the CNC (L), TC (L), CTC, and CTC (L) groups, with the CTC (L) group displaying more pronounced CRT exposure in comparison to the other groups. Furthermore, HMGB1 staining substantiated that the CTC (L) group had a marked release from the nucleus relative to other groups, the CTC (L) group showed higher ATP secrete than the control group (Fig. S15). Collectively, these findings corroborate the assertion that the CTC (L) group can induce a more potent ICD effect than other groups.

The recruitment of immune cells into the TME constitutes a pivotal parameter that bears a direct correlation with the anti-tumor immune response [56]. Accordingly, in a pursuit to ascertain whether mitochondria-targeted CTC micelles can augment their anti-tumor efficacy via the enhancement of immune cell infiltration, $CD8^+$ T cells within tumor tissues were subjected to immunofluorescence staining. As depicted in Fig. 6B, the infiltration of $CD8^+$ T cells (green) by the control and control (L) groups was negligible. Additionally, the NC (L), TC (L), CTC, and CTC (L) groups exhibited weak green fluorescence, denoting reduced $CD8^+$ T cells infiltration. Conversely, the CTC (L) group manifested a substantial number of infiltrated $CD8^+$ T cells within the tumor. In addition, we also measured the levels of $CD4^+$ and $CD8^+$ in the spleen and tumor tissue by flow cytometry. After treatment, mice were sacrificed for the determination of immune response. As shown in Fig. 6C–F, we found that compared with the control and CTC groups, CTC (L) treated spleen (Fig. 6C and E) and tumor (Fig. 6D and F) had the highest proportion of $CD4^+$ and $CD8^+$ T cells. The percentages of $CD3^+$ $CD8^+$ and $CD3^+$ $CD4^+$ T cells treated with CTC (L) were 4.00- and 2.09-fold higher than control in the spleen, respectively. The percentages of $CD3^+$ $CD8^+$ and $CD3^+$ $CD4^+$ T cells treated with CTC (L) were 2.09- and 1.59-fold higher than control in the tumor, respectively. Notably, Tregs

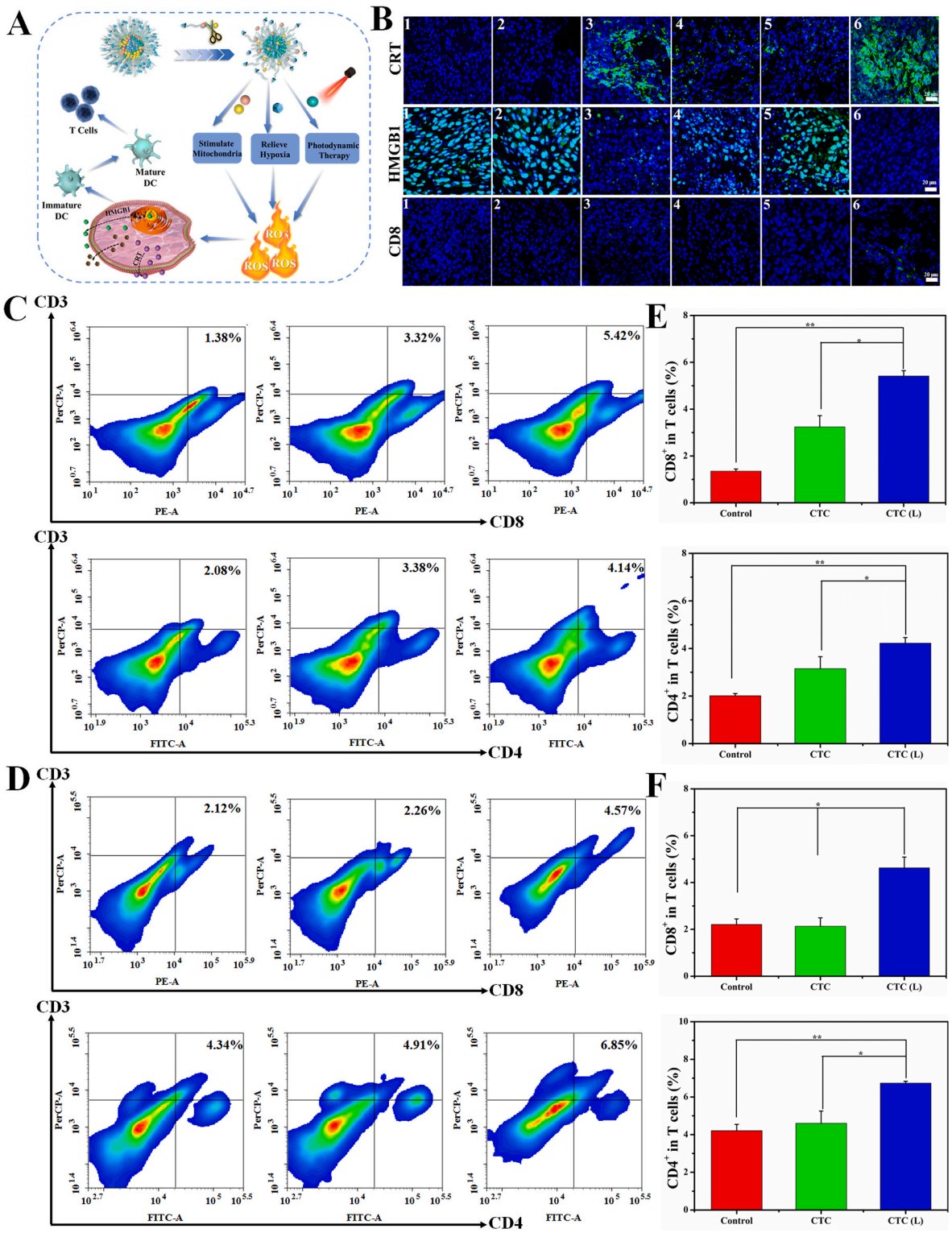

Fig. 6. (A) Schematic diagram of CTC micelles as ICD inducer integration platform to exert anti-cancer effect. (B) Immunofluorescence staining of CRT, HMGB1, and $CD8^+$ T cells in tumor tissues post-treatment with various groups. Representative plots of $CD3^+$ $CD8^+$ T cells and $CD3^+$ $CD4^+$ T cells in the (C) spleen and (D) tumor. The amount of $CD8^+$ and $CD4^+$ T cells in the (E) spleen and (F) tumor. $^*p < 0.05$ and $^{**}p < 0.01$, scale bar = 20 μm.

play a pivotal role in suppressing $CD8^+$ T cells and impeding DCs maturation, thereby fostering an immunosuppressive microenvironment [57]. Following CTC (L) treatment, we observed a noteworthy 10.78 % decrease in the proportion of Tregs in the treated group compared to the control group (Fig. S16). Subsequently, we conducted an in-depth analysis of immunostimulatory cytokines (IFN-γ, IL-6, and TNF-α) to assess the immune response triggered by CTC (L). As depicted in Fig. S17, the levels of these cytokines were significantly elevated in comparison to the control group. These results signifying that the fabricated CTC micelles can significantly amplify the immunogenicity of deceased tumor cells following light exposure, thereby eliciting an anti-tumor immune response.

To evaluate the abscopal effect of CTC (L)-mediated immune response, we constructed a bilateral tumor model to evaluate the abscopal effect of CTC (L)-mediated immune response. The right tumor was set as the primary tumor and the left tumor was designated as the distant tumor. Mice were randomly divided into 3 groups including control, CTC and CTC (L), with the CTC (L) group receiving laser irradiation of the primary tumor 36 h after tail vein injection, whereas the distant tumors were shielded from any treatments. As shown in Fig. 7, compared to the control and CTC groups, the CTC (L) group showed obvious inhibition effects on the tumor growth for both the primary tumor and distant tumor. This result indicate that CTC micelles can effectively initiate ICD-mediated immune response after laser irradiation, which has a good therapeutic efficacy for both the primary tumor and distant tumor.

3.8. Anti-tumor mechanism by transcriptomics analysis

On the basis of anti-tumor efficacy assays in vivo, in order to further explore the molecular mechanisms of CTC micelles therapeutic effect, we evaluated differentially expressed genes between the CTC (L) and the untreated control groups by transcriptomics analysis of 4T1 tumors. As shown in Fig. 8, CTC (L)-treated group induced a large number of genes expression fluctuations compared with the control group. Analysis revealed 1026 differentially expressed genes, 286 genes significantly downregulated and 780 genes markedly upregulated. Subsequently, Gene Ontology (GO) assessment was conducted on the aforementioned differentially expressed genes, revealing their significant ties to "biological process", "cellular component", and "molecular functions". Kyoto Encyclopedia of Genes and Genomes (KEGG) enrichment analysis was performed to determine the differences in biological processes and pathways among different samples. Multiple signaling pathways were significantly affected after treatment with CTC (L), including the MicroRNAs in Cancer, Rap1 signaling pathway, PI3K Akt signaling pathway, and Ras signaling pathway. Among which the PI3K Akt signaling pathway plays an important role in CRT exposure on the surface of cancer cells [58]. In addition, Tregs were considered a key type of immunosuppressive cell, often hijacked by the tumor microenvironment to evade immune response [59]. Foxp3 is considered a specific marker of Tregs, which is an intracellular transcription factor that determines the immunosuppressive phenotype of Tregs. Inhibition of Foxp3 can lead to the loss of immune suppression function of Tregs. Foxp3 was significantly downregulated after treatment with CTC (L), leading to the loss of immunosuppressive function of Tregs and effectively alleviating the immunosuppressive microenvironment. Collectively, these findings confirm that CTC (L) can effectively activate anti-tumor immunity and regulate immunosuppressive TME to enhance cancer immunity.

3.9. Biosafety evaluation

The inherent biocompatibility of polymer micelles serves as a foundational cornerstone for their efficacy in vivo, and as such, the biosafety of polymer micelles was the subject of an exhaustive investigation through an array of experimental procedures. Initially, the cytotoxicity of CTC micelles upon human normal hepatocytes (LO2) was scrutinized by employing MTT assay. As delineated in Fig. S18A, subsequent to a 24 h treatment with a concentration of 43 μg/mL CTC micelles, the viability of LO2 cells persisted at levels exceeding 85 %. Such findings are indicative of the commendable biocompatibility inherent in the formulated CTC micelles. Following this, in vitro hemolysis assay was conducted, as documented in Fig. S18B. Remarkably, the hemolysis rate was found to be less than 1 % even at a concentration of 43 μg/mL of CTC micelles, a further testament to the CTC micelles' favorable hemocompatibility. Subsequently, comprehensive hematological and biochemical assessments were undertaken. As illustrated in Figs. S18C–18E no statistically significant deviations were observed in liver function markers (ALT, AST, ALP), and renal function markers (BUN, CRE), or hematological parameters when juxtaposed with the control group. Lastly, key organs (namely the heart, liver, spleen, lung, and kidney) from mice across various treatment groups were harvested for H&E staining. The absence of discernible pathological alterations (Fig. S18) points to the fact that polymer micelles exhibited minimal toxic side effects during their accumulation within major mice organs.

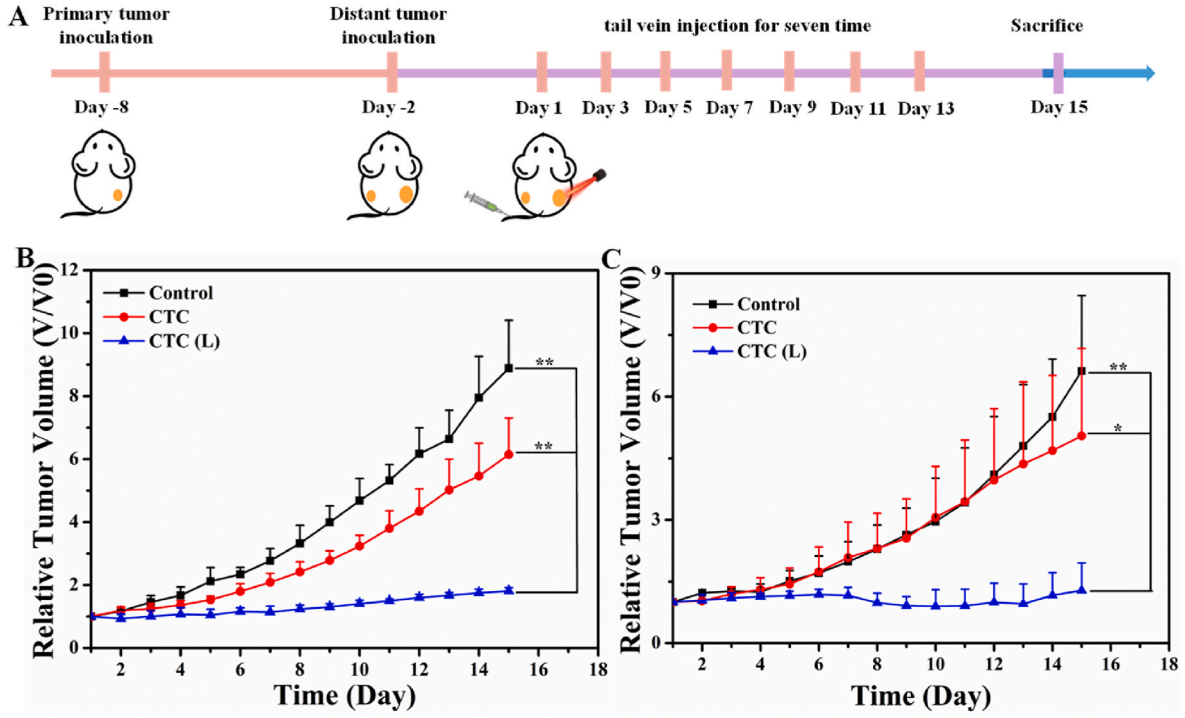

Fig. 7. Abscopal antitumor effect in vivo. (A) Experimental design of treatment. Relative tumor volume of the (B) primary and (C) distant tumors in different treatment groups (n = 4). *$p < 0.05$ and **$p < 0.01$.

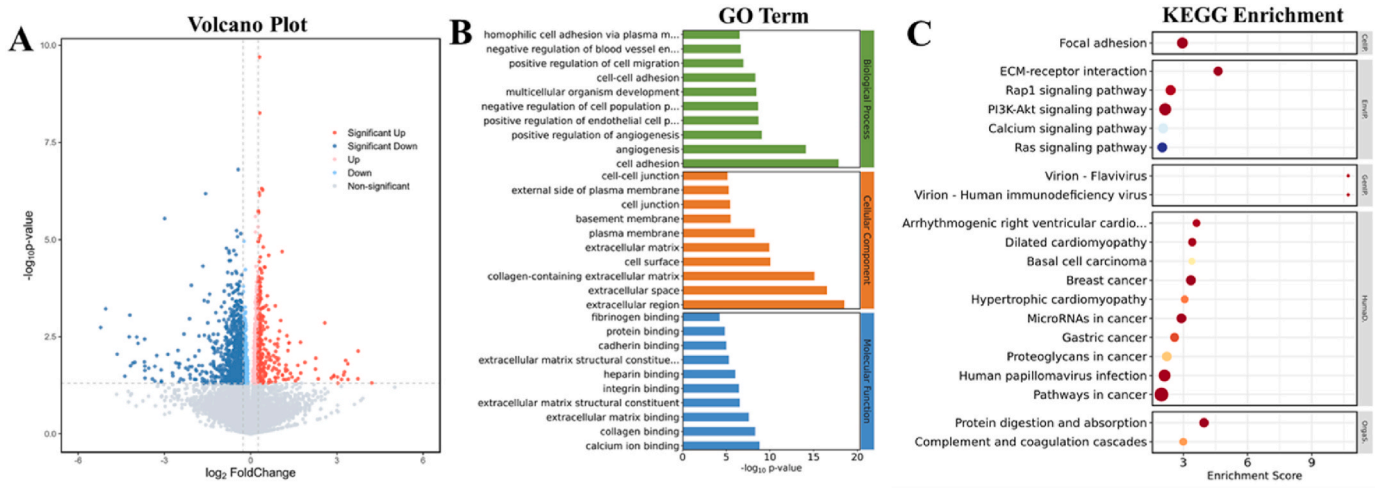

Fig. 8. (A) Differentially expressed genes between the CTC (L)-treated and the untreated control groups are represented on a volcano plot map. (B) GO enrichment analysis and (C) KEGG pathway enrichment analysis of differentially expressed genes treated with PBS and CTC (L), respectively; n = 5.

The cumulative evidence garnered from these analyses consolidates the assertion that CTC micelles possess an elevated level of therapeutic biosafety. This is principally attributable to the precision delivery of tumor-targeted drugs, thereby mitigating the adverse effects upon non-tumor organs.

4. Conclusion

The study at hand presents a meticulous synthesis of a ROS-responsive and triple-synergistic mitochondria-targeted polymeric micelle construct (CTC micelle), specifically architected to function as a multi-stage amplifier of ROS, with a goal to efficaciously trigger ICD by inducing the domino effect. In the initial phase of development, the mitochondrial-targeted micelles were fabricated via ethanol injection, a process during which CAT was meticulously encapsulated within the micelle's architecture. This encapsulation was performed during the micelle's self-assembly phase, thus laying the groundwork for enhanced PDT, achievable under laser irradiation at a wavelength of 660 nm. Such a methodological approach was instrumental in dramatically augmenting the efficiency of ROS generation. Both in vitro and in vivo experimental paradigms were employed to substantiate that CTC micelles possess the capability to effectively incite the production of ROS, thereby laying an empirical foundation for the effective induction of ICD. Further in vitro and in vivo assays have illuminated that CTC micelles can actively induce the exposure of CRT and the liberation of HMGB1 ATP. Such a phenomenon is concomitant with a significant amplification of $CD8^+$ T cells infiltration within tumors, a vital step in reversing the tumor's immunosuppressive microenvironment. In summation, the data presented herein unambiguously underscore the potential therapeutic value that CTC micelles could offer within the ambit of cancer therapeutics.

Ethics approval and consent to participate

All animal experiments were approved by the Ethics Committee of the Animal Experimental Center of Hebei Medical University (Checking number: 2023032), and were carried out in compliance with all relevant ethical regulations.

Data availability

Data will be made available on request.

CRediT authorship contribution statement

Xiaoxiao Hu: Writing – original draft, Validation, Methodology, Investigation, Data curation. **Mo Zhang:** Writing – review & editing, Visualization, Supervision, Funding acquisition. **Cuilu Quan:** Software, Investigation, Data curation. **Saisai Ren:** Validation, Software, Data curation. **Wei Chen:** Writing – review & editing, Visualization, Supervision. **Jing Wang:** Writing – review & editing, Visualization, Supervision, Funding acquisition, Conceptualization.

Declaration of competing interest

The authors declare that they have no known competing financial interests or personal relationships that could have appeared to influence the work reported in this paper.

Acknowledgements

The authors gratefully acknowledge the financial support from the National Natural Science Foundation of China (Grants No. 22301060), the Youth Top Talent Project of Hebei Province Higher Education (No. BJK2024190), the Natural Science Foundation of Hebei Province (No. H2020206416, B2020206007), the Post-graduate's Innovation Fund Project of Hebei Province (No. CXZZBS2023104), the Postdoctoral Fund and of Hebei Medical University, the Chunyu Project Outstanding Youth Fund of Hebei Medical University (No. CYYQ2023004) and the China Postdoctoral Science Foundation (No. 2023TQ0103 and 2023M730914). In this work we thank Hebei Medical University Core Facilities and Centers.

Appendix A. Supplementary data

Supplementary data to this article can be found online at https://doi.org/10.1016/j.bioactmat.2024.06.038.

References

[1] H. Deng, Z. Zhou, W. Yang, L. Lin, S. Wang, G. Niu, J. Song, X. Chen, Endoplasmic reticulum targeting to amplify immunogenic cell death for cancer immunotherapy, Nano Lett. 20 (3) (2020) 1928–1933.
[2] X. Deng, Z. Shao, Y. Zhao, Solutions to the drawbacks of photothermal and photodynamic cancer therapy, Adv. Sci. 8 (2021) 2002504.
[3] J. Fucikova, O. Kepp, L. Kasikova, G. Petroni, T. Yamazaki, P. Liu, L. Zhao, R. Spisek, G. Kroemer, L. Galluzzi, Detection of immunogenic cell death and its relevance for cancer therapy, Cell Death Dis. 11 (2020) 1013.

[4] B. Hernández, Y. Yu, F. Ossendorp, M. Korbelik, S. Oliveira, Preclinical and clinical evidence of immune responses triggered in oncologic photodynamic therapy: clinical recommendations, J. Clin. Med. 9 (2) (2020) 333.

[5] G. Abhishek, Damage-associated molecular patterns: revealing the molecular communication between dying cancer cells and the immune system, Acta Biomed. 583 (2012) 124.

[6] M. Zha, G. Yang, Y. Li, C. Zhang, B. Li, K. Li, Recent advances in AIEgen-based photodynamic therapy and immunotherapy, Adv. Healthcare Mater. 10 (24) (2021) 2101066.

[7] S. Jia, Z. Gao, Z. Wu, H. Gao, H. Wang, H. Ou, D. Ding, Sonosensitized aggregation-induced emission dots with capacities of immunogenic cell death induction and multivalent blocking of programmed cell death-ligand 1 for amplified antitumor immunotherapy, CCS Chem. 4 (2) (2022) 501–514.

[8] Y. Yang, F. Chen, N. Xu, Q. Yao, R. Wang, X. Xie, F. Zhang, Y. He, D. Shao, W. Dong, J. Fan, W. Sun, X. Peng, Red-light-triggered self-destructive mesoporous silica nanoparticles for cascade-amplifying chemo-photodynamic therapy favoring antitumor immune responses, Biomaterials 281 (2022) 121368.

[9] D. Wei, Y. Chen, Y. Huang, P. Li, Y. Zhao, X. Zhang, J. Wan, X. Yin, T. Liu, J. Yin, Z. Liu, Q. Zhang, J. Wang, H. Xiao, NIR-light triggered dual-cascade targeting core-shell nanoparticles enhanced photodynamic therapy and immunotherapy, Nano Today 41 (2021) 101288.

[10] B. Feng, B. Hou, Z. Xu, M. Saeed, H. Yu, Y. Li, Self-amplified drug delivery with light-inducible nanocargoes to enhance cancer immunotherapy, Adv. Mater. 31 (40) (2019) 1902960.

[11] C. Chen, X. Ni, S. Jia, Y. Liang, X. Wu, D. Kong, D. Ding, Massively evoking immunogenic cell death by focused mitochondrial oxidative stress using an AIE luminogen with a twisted molecular structure, Adv. Mater. 31 (52) (2019) 1904914.

[12] X. Xu, J. Duan, Y. Liu, Y. Kuang, J. Duan, T. Liao, Z. Xu, B. Jiang, C. Li, Multi-stimuli responsive hollow MnO_2-based drug delivery system for magnetic resonance imaging and combined chemo-chemodynamic cancer therapy, Acta Biomater. 126 (2021) 445–462.

[13] J. Zhai, J. Gao, J. Zhang, D. Liu, S. Gao, Y. Yan, K. Zhang, K. Cai, F. Yu, M. Lin, J. Li, Concave octahedral PtCu nanoframes mediated synergetic photothermal and chemodynamic tumor therap, Chem. Eng. J. 442 (2) (2022) 136172.

[14] M. Aioub, S. Panikkanvalappil, M. El-Sayed, Platinum-coated gold nanorods: efficient reactive oxygen scavengers that prevent oxidative damage toward healthy, untreated cells during plasmonic photothermal therapy, ACS Nano 11 (1) (2017) 579–586.

[15] S. Feng, J. Lu, K. Wang, D. Di, Z. Shi, Q. Zhao, S. Wang, Advances in smart mesoporous carbon nanoplatforms for photothermal-enhanced synergistic cancer therapy, Chem. Eng. J. 435 (2) (2022) 134886.

[16] H. He, L. Du, H. Xue, J. Wu, X. Shuai, Programmable therapeutic nanoscale covalent organic framework for photodynamic therapy and hypoxia-activated cascade chemotherapy, Acta Biomater. 149 (2022) 297–306.

[17] H. Song, Z. Cai, J. Li, H. Xiao, R. Qi, M. Zheng, Light triggered release of a triple action porphyrin-cisplatin conjugate evokes stronger immunogenic cell death for chemotherapy, photodynamic therapy and cancer immunotherapy, J. Nanobiotechnol. 20 (329) (2022) 1–11.

[18] G. Yang, L. Xu, J. Xu, R. Zhang, G. Song, Y. Chao, L. Feng, F. Han, Z. Dong, B. Li, Z. Liu, Smart nanoreactors for pH-responsive tumor homing, mitochondria-targeting, and enhanced photodynamic-immunotherapy of cancer, Nano Lett. 18 (4) (2018) 2475–2484.

[19] J. Lu, Y. Mao, S. Feng, X. Li, Y. Gao, Q. Zhao, S. Wang, Biomimetic smart mesoporous carbon nanozyme as a dual-GSH depletion agent and O_2 generator for enhanced photodynamic therapy, Acta Biomater. 148 (2022) 310–322.

[20] L. Shi, P. Zhang, X. Liu, Y. Li, W. Wu, X. Gao, B. Liu, An activity-based photosensitizer to reverse hypoxia and oxidative resistance for tumor photodynamic eradication, Adv. Mater. 34 (45) (2022) 2206659.

[21] J. Xu, L. Xu, C. Wang, R. Yang, Q. Zhuang, X. Han, Z. Dong, W. Zhu, R. Peng, Z. Liu, Near-infrared-triggered photodynamic therapy with multitasking upconversion nanoparticles in combination with checkpoint blockade for immunotherapy of colorectal cancer, ACS Nano 11 (5) (2017) 4463–4474.

[22] S. Zeng, C. Chen, L. Zhang, X. Liu, M. Qian, H. Cui, J. Wang, Q. Chen, X. Peng, Activation of pyroptosis by specific organelle-targeting photodynamic therapy to amplify immunogenic cell death for anti-tumor immunotherapy, Bioact. Mater. 25 (2023) 580–593.

[23] Y. Li, J. Hu, X. Liu, Y. Liu, S. Lv, J. Dang, Y. Ji, J. He, L. Yin, Photodynamic therapy-triggered on-demand drug release from ROS-responsive core-cross-linked micelles toward synergistic anti-cancer treatment, Nano Res. 12 (2019) 999–1008.

[24] W. Pan, Y. Tan, W. Meng, N. Huang, Y. Zhao, Z. Yu, Z. Huang, W. Zhang, B. Sun, J. Chen, Microenvironment-driven sequential ferroptosis, photodynamic therapy, and chemotherapy for targeted breast cancer therapy by a cancer-cell-membrane-coated nanoscale metal-organic framework, Biomaterials 283 (2022) 121449.

[25] Z. Zhang, R. Wang, R. Luo, J. Zhu, X. Huang, W. Liu, F. Liu, F. Feng, W. Qu, An activatable theranostic nanoprobe for dual-modal imaging-guided photodynamic therapy with self-reporting of sensitizer activation and therapeutic effect, ACS Nano 15 (3) (2021) 5366–5383.

[26] J. Brown, W. Wilson, Exploiting tumor hypoxia in cancer treatment, Nat. Rev. Cancer 4 (2004) 437–447.

[27] L. Hai, A. Zhang, X. Wu, H. Cheng, D. He, T. Wang, X. He, K. Wang, Liposome-stabilized black phosphorus for photothermal drug delivery and oxygen self-enriched photodynamic therapy, ACS Appl. Nano Mater. 3 (1) (2019) 563–575.

[28] R. Tan, J. Ge, C. Wang, Y. Wan, X. Yang, Diselenide-triggered hydroxyethyl starch conjugate nanoparticles with cascade drug release properties for potentiating chemo-photodynamic therapy, Carbohydr. Polym. 311 (2023) 120748.

[29] Y. Zhou, F. Tong, W. Gu, S. He, X. Yang, J. Li, Y. Gao, H. Gao, Co-delivery of photosensitizer and diclofenac through sequentially responsive bilirubin nanocarriers for combating hypoxic tumors, Acta Pharm. Sin. B 12 (3) (2022) 1416–1431.

[30] Q. Sun, H. Bi, Z. Wang, C. Li, C. Wang, J. Xu, D. Yang, F. He, S. Gai, P. Yang, O_2-generating metal-organic framework-based hydrophobic photosensitizer delivery system for enhanced photodynamic therapy, ACS Appl. Mater. Interfaces 11 (40) (2019) 36347–36358.

[31] J. Shen, H. Yu, Y. Shu, M. Ma, H. Chen, A robust ROS generation strategy for enhanced chemodynamic/photodynamic therapy via H_2O_2/O_2 self-supply and Ca^{2+} overloading, Adv. Funct. Mater. 31 (50) (2021) 2106106.

[32] Y. Cheng, Y. Ji, J. Tong, Triple stimuli-responsive supramolecular nanoassembly with mitochondrial targetability for chemophotothermal therapy, J. Contr. Release 327 (2020) 35–49.

[33] W. Zhang, X. Hu, Q. Shen, D. Xing, Mitochondria-specific drug release and reactive oxygen species burst induced by polyprodrug nanoreactors can enhance chemotherapy, Nat. Commun. 10 (2019) 1–14.

[34] N. Sen, B. Das, A. Ganguly, T. Mukherjee, G. Tripathi, S. Bandyopadhyay, S. Rakshit, T. Sen, H.K. Majumder, Camptothecin induced mitochondrial dysfunction leading to programmed cell death in unicellular hemoflagellate Leishmania donovani, Cell Death Differ. 11 (2004) 924–936.

[35] Y. Wang, T. Zhang, C. Hou, M. Zu, Y. Lu, X. Ma, D. Jia, P. Xue, Y. Kang, Z. Xu, Mitochondria-specific anticancer drug delivery based on reduction-activated polyprodrug for enhancing the therapeutic effect of breast cancer chemotherapy, ACS Appl. Mater. Interfaces 11 (2019) 29330–29340.

[36] B. Wang, K. Chen, Q. Zhang, L. Gu, Q. Luo, Z. Li, Q. Gong, H. Zhang, Z. Gu, K. Luo, ROS-responsive amphiphilic block copolymer-drug conjugate: design, synthesis and potential as an efficient drug delivery system via a positive feedback strategy, Chem. Eng. J. 425 (2021) 131453.

[37] Y. Tu, X. Xiao, Y. Dong, J. Li, Y. Liu, Q. Zong, Y. Yuan, Cinnamaldehyde-based poly (thioacetal): a ROS-awakened self-amplifying degradable polymer for enhanced cancer immunotherapy, Biomaterials 289 (2022) 121795.

[38] J. Noh, B. Kwon, E. Han, M. Park, W. Yang, W. Cho, W. Yoo, G. Khang, D. Lee, Amplification of oxidative stress by a dual stimuli-responsive hybrid drug enhances cancer cell death, Nat. Commun. 6 (1) (2015) 6907.

[39] T. Zhao, C. Liang, Y. Zhao, X. Xue, Z. Ma, J. Qi, H. Shen, S. Yang, J. Zhang, Q. Jia, Q. Du, D. Cao, B. Xiang, H. Zhang, X. Qi, Multistage pH-responsive codelivery liposomal platform for synergistic cancer therapy, J. Nanobiotechnol. 20 (2022) 177.

[40] J. Zhuang, B. Wang, H. Chen, K. Zhang, N. Li, N. Zhao, B. Tang, Efficient NIR-II type-I AIE photosensitizer for mitochondria-targeted photodynamic therapy through synergistic apoptosis-ferroptosis, ACS Nano 17 (10) (2023) 9110–9125.

[41] J. Sun, J. Li, X. Li, L. Yang, Y. Liu, H. Gao, L. Xiang, Sequentially responsive size reduction and drug release of core-satellite nanoparticles to enhance tumor penetration and effective tumor suppression, Chin. Chem. Lett. 34 (5) (2023) 107891.

[42] C. Yue, Y. Yang, C. Zhang, G. Alfranca, S. Cheng, L. Ma, Y. Liu, X. Zhi, J. Ni, W. Jiang, J. Song, J. Fuente, D. Cui, ROS-responsive mitochondria-targeting blended nanoparticles: chemo-and photodynamic synergistic therapy for lung cancer with on-demand drug release upon irradiation with a single light source, Theranostics 6 (13) (2016) 2352–2366.

[43] Z. Mao, X. Bi, C. Yu, L. Chen, J. Shen, Y. Huang, Z. Wu, H. Qi, J. Guan, X. Shu, Mechanically robust and personalized silk fibroin-magnesium composite scaffolds with water-responsive shape-memory for irregular bone regeneration, Nat. Commun. 15 (1) (2024) 4160.

[44] J. Lan, L. Liu, R. Zeng, Y. Qin, J. Hou, S. Xie, S. Yue, J. Yang, R. Ho, Y. Ding, T. Zhang, Tumor-specific carrier-free nanodrugs with GSH depletion and enhanced ROS generation for endogenous synergistic anti-tumor by a chemotherapy-photodynamic therapy, Chem. Eng. J. 407 (2021) 127212.

[45] W. Li, Z. Wang, S. Hao, H. He, Y. Wan, C. Zhu, L. Sun, G. Cheng, S. Zheng, Mitochondria-targeting polydopamine nanoparticles to deliver doxorubicin for overcoming drug resistance, ACS Appl. Mater. Interfaces 9 (20) (2017) 16793–16802.

[46] Z. Peng, K. Ning, X. Tang, R. He, D. Zhang, Y. Ma, S. Guan, J. Zhai, A multifunctional DNA repair enzyme and magnetic dual-triggered theranostic nanosystem for intelligent drug delivery, Mater. Des. 226 (2023) 111611.

[47] K. Sun, Z. Gao, Y. Zhang, H. Wu, C. You, S. Wang, P. An, C. Sun, B. Sun, Enhanced highly toxic reactive oxygen species levels from iron oxide core-shell mesoporous silica nanocarrier-mediated Fenton reactions for cancer therapy, J. Mater. Chem. B 6 (37) (2018) 5876–5887.

[48] L. Liu, C. Li, J. Gong, Y. Zhang, W. Ji, L. Feng, G. Jiang, J. Wang, B. Tang, A highly water-soluble aggregation-induced emission luminogen with anion-π^+ interactions for targeted nir imaging of cancer cells and type I photodynamic therapy, Angew. Chem. 135 (33) (2023) e202307776.

[49] Y. Wang, S. Luo, Y. Wu, P. Tang, J. Liu, Z. Liu, S. Shen, H. Ren, D. Wu, Highly penetrable and on-demand oxygen release with tumor activity composite nanosystem for photothermal/photodynamic synergetic therapy, ACS Nano 14 (12) (2020) 17046–17062.

[50] B. Huang, J. Gao, Application of 3D cultured multicellular spheroid tumor models in tumor-targeted drug delivery system research, J. Contr. Release 270 (2018) 246–259.

[51] S. Lu, X. Lei, H. Ren, S. Zheng, J. Qiang, Z. Zhang, Y. Chen, T. Wei, F. Wang, X. Chen, PEGylated dimeric BODIPY photosensitizer as nanocarrier for combined chemotherapy and cathepsin B-activated photodynamic therapy in 3D tumor spheroids, ACS Appl. Bio Mater. 6 (2020) 3835–3845.

[52] H. Zhang, Q. Zhang, Z. Guo, K. Liang, C. Boyer, J. Liu, Z. Zheng, R. Amal, S. Yun, Z. Gu, Disulfiram-loaded metal organic framework for precision cancer treatment via ultrasensitive tumor microenvironment-responsive copper chelation and radical generation, J. Colloid Interface Sci. 615 (2022) 517–526.
[53] F. Tong, H. Hu, Y. Xu, Y. Zhou, R. Xie, T. Lei, Y. Du, W. Yang, S. He, Y. Huang, Hollow copper sulfide nanoparticles carrying ISRIB for the sensitized photothermal therapy of breast cancer and brain metastases through inhibiting stress granule formation and reprogramming tumor-associated macrophages, Acta Pharm. Sin. B 13 (8) (2023) 3471–3488.
[54] Q. Sun, Z. Yang, M. Lin, Y. Peng, R. Wang, Y. Du, Y. Zhou, J. Li, X. Qi, Phototherapy and anti-GITR antibody-based therapy synergistically reinvigorate immunogenic cell death and reject established cancers, Biomaterials 269 (2021) 120648.
[55] X. Jiao, L. Sun, W. Zhang, J. Ren, L. Zhang, Y. Cao, Z. Xu, Y. Kang, P. Xue, Engineering oxygen-deficient ZrO_2-x nanoplatform as therapy-activated "immunogenic cell death (ICD)" inducer to synergize photothermal-augmented sonodynamic tumor elimination in NIR-II biological window, Biomaterials 272 (2021) 120787.
[56] J. Zheng, J. Sun, J. Chen, S. Zhu, S. Chen, Y. Liu, L. Hao, Z. Wang, S. Chang, Oxygen and oxaliplatin-loaded nanoparticles combined with photo-sonodynamic inducing enhanced immunogenic cell death in syngeneic mouse models of ovarian cancer, J. Contr. Release 332 (2021) 448–459.
[57] Y. Du, Y. Guo, X. Xiao, X. Zhu, Y. Liu, X. Ruan, X. Huang, Y. Yuan, X. Wei, Glutathione depletion and photosensitizer activation augments efficacy of tumor photodynamic immunotherapy, Chem. Eng. J. 442 (1) (2022) 136170.
[58] H. Liu, Y. Hu, Y. Sun, C. Wan, Z. Zhang, X. Dai, Z. Lin, Q. He, Z. Yang, P. Huang, Y. Xiong, J. Cao, X. Chen, Q. Chen, J. Lovell, Z. Xu, H. Jin, K. Yang, Co-delivery of bee venom melittin and a photosensitizer with an organic-inorganic hybrid nanocarrier for photodynamic therapy and immunotherapy, ACS Nano 13 (11) (2019) 12638–12652.
[59] J. Guo, Q. An, M. Guo, Y. Xiao, B. Li, F. Gao, Y. Wang, J. Li, Y. Wang, Y. Liu, H. Meng, J. Guo, J. Liu, Oxygen-independent free radical generation mediated by core-shell magnetic nanocomposites synergizes with immune checkpoint blockade for effective primary and metastatic tumor treatment, Nano Today 36 (2021) 101024.